PHILOSOPHICAL TRANSACTIONS OF THE ROYAL SOCIETY A MATHEMATICAL, PHYSICAL & ENGINEERING SCIENCES

On Acoustic Transmission in Ocean-Surface Waveguides

M. J. Buckingham

Phil. Trans. R. Soc. Lond. A 1991 **335**, 513-555
doi: 10.1098/rsta.1991.0059

On acoustic transmission in ocean-surface waveguides

By M. J. Buckingham

Marine Physical Laboratory, Scripps Institution of Oceanography, La Jolla, California 92093, U.S.A., and Institute of Sound and Vibration Research, The University, Southampton SO9 5NH, U.K.

CONTENTS

	PAGE
1. Introduction	515
2. Theory: propagation in an inverse-square profile	518
3. Discrete and continuous components of the field	522
4. The modal field	523
4.1. The Hankel function $H^{(1)}_{-j\nu}(j\sigma)$	524
4.2. The Hankel function $H^{(2)}_{-j\nu}(j\sigma)$	526
4.3. Physical properties of the normal modes	527
4.4. The mode sum	528
4.5. Interference wavelength	530
5. Arctic Ocean acoustics	531
5.1. VLF propagation	531
5.1.1. Multimode suppression and mode interference	532
5.1.2. Power spectral density	534
5.1.3. Infrasonic ambient noise	534
5.2. Ocean-acoustic tomography: Greenland Sea experiment	536
5.2.1. Group velocity of the modes	536
6. Ambient sound in a bubbly surface duct	538
6.1. Theory: La Perouse	541
6.2. Theory: FASINEX	542
6.3. Interpretation of the wave-breaking spectra	544
6.4. Inverse solution for the source depth	545
6.5. Alternative mechanisms	546
7. Concluding remarks	547
Appendix A. Normal modes and the branch line integral	548
Appendix B. Asymptotic analyses of $H^{(1)}_{-j\nu}(j\sigma)$	550
Appendix C. Spectral periodicity in the mode sum	552
References	553

A sound speed profile which increases monotonically with depth below the ocean surface is upward-refractive, acting as a duct in which sound may be transmitted to long ranges with little attenuation. A well-known example is the mixed layer, in which the temperature is uniform and the sound speed approximately scales with the hydrostatic pressure, increasing linearly with depth. The depth of the mixed layer depends on surface conditions, but is of the order of 100 m. Deeper channels are

Phil. Trans. R. Soc. Lond. A (1991) **335**, 513–555
Printed in Great Britain

found in ice-covered polar waters, where the temperature and sound speed profiles both show a minimum at the surface. A typical surface duct in the Arctic Ocean may extend to depths of 1000 m or more and is capable of supporting very-low-frequency (VLF) (1–50 Hz) acoustic transmissions with no bottom interactions. On a depth scale that is smaller by several orders of magnitude, wave-breaking events create a bubbly layer one or two metres thick below the sea surface, with the highest concentration of bubbles, and correspondingly the lowest sound speed, at the surface. The bubble layer acts as a waveguide for sound in the audio frequency range, above 2 kHz, although transmission may be severely attenuated due to absorption and scattering by the bubbles, as well as by the irregular geometry of the sea surface and the bubble clouds.

Most ocean-surface waveguides can be accurately represented by an inverse-square sound speed profile, which may be monotonic increasing (upward refracting) or decreasing (downward refracting) with depth, and whose detailed shape is governed by just three parameters. An analysis of the sound field below the sea surface in the presence of such a profile shows that it consists of a near-field component, given by a branch-line integral, plus a sum of uncoupled normal modes representing the trapped radiation which propagates to longer ranges. The modal contribution is identically zero in the case of the downward refracting profiles. The properties of the modes emerge from a straightforward theoretical development involving first- and second-order asymptotics: each mode shows an oscillatory region immediately below the surface, terminating at the extinction depth, below which the mode decays exponentially to zero; the extinction depth increases rapidly with both mode number and the reciprocal of the acoustic frequency; a reciprocal relationship exists between the extinction depth and the mode strength; and there is no mode cut-off, nor are there any evanescent modes.

On applying the inverse-square theory to VLF Arctic Ocean transmissions, the spectral density of the modal field is found to show a steep positive gradient between 5 and 50 Hz, the rising level occurring as more modes make a significant contribution to the field. This result is compared with observations of infra-sonic ambient noise that have been made in the marginal ice zone of the Greenland Sea, using surface suspended, flow-shielded hydrophones. The measured spectra show a deep minimum at about 5 Hz, in accord with the theoretical prediction.

The inverse-square theory also has application to under-ice ocean-acoustic tomography, where the dispersive nature of the upward refractive channel governs the arrival times of the modes at the receivers. A simple expression for the group velocity of the modes gives the arrival times. More generally, the full modal structure of the field across the tomography array may be constructed from the theory.

Acoustic signatures of wave-breaking events have recently been observed in the ocean-surface bubble layer by Farmer & Vagle (1989). The spectra show well-defined peaks (La Perouse) or a broader-band structure (FASINEX), both of which are fully explained, in terms of intermode interference, by the inverse-square theory. The differences between the two data-sets are attributed to the different sound speed profiles in the bubble layers at the two sites. The spectral banding in FASINEX is a modulation phenomenon, showing a strong dependence on the source depth. A straightforward inverse calculation indicates that the bubble sources in FASINEX are located at a depth of 1.5 m, corresponding roughly to the base of the bubble layer. This is a slightly unexpected conclusion, since acoustically active bubbles generated by spilling breakers under wind-free conditions in a laboratory tank are known to be

located within a few millimetres of the surface. However, aeration is much more pronounced at the wind-driven surface of the ocean than in a tank, which may be a factor in accounting for the deeper sources. There are practical difficulties in measuring the source distribution using conventional techniques, but the inverse-square transmission theory in conjunction with near-surface measurements of wave-breaking signatures provides an effective means of making such a determination.

1. Introduction

When the sound speed in the ocean increases monotonically with depth, the medium is upward refracting and acts as a subsurface waveguide along which sound may propagate to long distances with little attenuation. An example of such a duct may be found under the ice cover in the Arctic Ocean (Urick 1983), where the surface waters are maintained near freezing (−2 °C), the temperature increases with depth, and the sound speed profile shows a minimum at the surface. In this environment the 'surface' channel, that is the region where the sound speed shows a positive gradient, may extend throughout the water column to a depth of several thousand metres, and is capable of supporting very-low-frequency (VLF) (1–50 Hz) sound transmission, with negligible bottom interaction, to ranges of hundreds of kilometres.

A similar sound speed profile, but with substantially smaller length scale, occurs within ten metres or so of the surface of the open ocean, in the presence of breaking waves. Thorpe (1982, 1984*a*) observed that air entrained by waves diffuses downwards by the action of turbulence, to form a subsurface layer of bubble clouds. The volume fraction of air in this bubbly layer decays with depth (Thorpe 1984*b*), as a result of which the sound speed increases with depth, thus providing the upward refracting condition necessary for acoustic ducting to occur. The surface sound channel formed through wave-breaking is capable of supporting acoustic frequencies in the audio band from two to several tens of kilohertz; but long-range propagation in this case may be limited by scattering and absorption of sound by the entrained bubbles, and by the irregular structure of the bubble layer.

Acoustic techniques have immense potential for investigating and monitoring sea-surface processes such as ice fracturing in the Arctic, or gas exchange across the air–sea interface through wave-breaking on the open ocean. In such applications of acoustics the propagation conditions in the surface sound channel will almost certainly influence the observations, implying that a simple interpretation based on straight-line propagation is likely to be misleading. Although this would appear to be a drawback of acoustics, in point of fact the opposite is true: the complicated structure imposed on the signal by the anisotropic medium represents *information*. Strategies designed to extract this information rely heavily on an ability to predict with precision the effects of the transmission path on the received signal.

Several numerical, acoustic-propagation-loss algorithms are available (Harrison 1989), representing one means of investigating acoustic fields in the ocean. A preferable approach, at least in principle, is an analytical treatment of the problem, analogous to Pekeris's (1948) classic analysis of the acoustic field in a two-layered liquid half-space in which the sound speed and density are discontinuous at the interface. But theories of radiation fields in smoothly varying, non-uniform (sound speed or refractive index) profiles usually involve a mathematical development that rapidly becomes intractable.

PHILOSOPHICAL TRANSACTIONS OF THE ROYAL SOCIETY A MATHEMATICAL, PHYSICAL & ENGINEERING SCIENCES

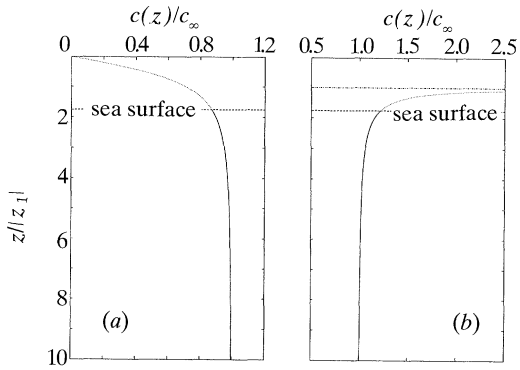

Figure 1. The (normalized) (*a*) upward refracting and (*b*) downward refracting inverse-square profiles. Only the portions below the sea surface (solid curves) are relevant to the ocean-acoustic propagation problem.

However, certain profiles are amenable to some degree of analysis, including, for example, the bilinear refractive index profile that was first investigated by Furry (1951), in connection with the transmission of radio waves in atmospheric ducts, and which was subsequently applied to ocean-acoustic propagation by Labianca (1973). In a similar vein, Pederson & Gordon (1965, 1970) implemented normal mode theory in an analysis of sound propagation in surface ducts. By using a somewhat different approach, but applied to the same type of environment, Weston (1986) established the effect of source depth on acoustic intensity in a surface channel. The acoustic properties of deeper channels have also been investigated analytically, notably by Überall & Nicholas (1968), who had some success in predicting range focusing effects in a parabolic profile.

In the present work, the so-called inverse-square profile (Felsen & Marcuvitz 1973) is examined in a theoretical treatment of sound transmission in a surface sound channel. The sound speed, $c(z)$, in the inverse-square ocean, as a function of the depth coordinate, z, is given by the expression

$$1/c^2(z) = (1/c_\infty^2)\{1 + z_1^2/z^2\}, \tag{1}$$

where the parameter c_∞ is the value of $c(z)$ in the limit as $z \to \infty$. For the profile to have a positive gradient the second parameter, z_1, in equation (1) must be real; if z_1 is imaginary, the gradient is negative and the profile is downward refracting, in which case normal mode propagation is not supported.

Figure 1 shows the upward and downward refracting forms of the inverse-square profile. In figure 1*a* (z_1 real) the sound speed is seen to be zero when $z = 0$, a condition which is not normally encountered at the sea surface. This minor difficulty is avoided by positioning the surface below the origin of z at

$$z = z_s \geqslant 0, \tag{2}$$

thus allowing the sound speed at the surface to be finite. The depth coordinate, z_s, of the surface is the third and final parameter required to characterize completely the inverse-square profile.

When z_1 is imaginary, the sound speed given in equation (1) diverges to infinity at a depth equal to the magnitude of z_1 and is imaginary at shallower depths. In this case, to assure a physically realizable profile, the sea surface must satisfy the

condition $z_s > |z_1|$. Below the surface the profile is then real with a negative gradient (figure 1*b*). Although not of immediate interest, this downward refracting version of the inverse-square profile has been included here since it is automatically accommodated by the field analysis to follow.

Two special cases of the inverse-square profile are the isospeed (i.e. non-refracting) profile ($z_1 = 0$), which will be useful later as a check on some of the mathematical developments, and the linear (i.e. constant gradient) profile (Pekeris 1946). The latter is obtained from (1) by setting $z_1 \propto c_\infty$ and letting $c_\infty \to \infty$, and is distinct from a profile in which the square of the refractive index is either linear in z, a problem discussed by Jones (1986) and Li *et al.* (1990), or of a quadratic form (Jeng & Liu 1987).

In general, the inverse-square profile shows some curvature and with a judicious choice of parameters is accurately representative of various surface sound channels, including those in the Arctic Ocean and the surface bubble layer. We shall see later that in the upward refracting profile, z_1 is a measure of the 'effective' depth of the surface channel, in the sense of being, along with frequency, the factor controlling the number of significant modes supported by the profile.

The problem of determining the sound field from a point source in an inverse-square ocean is tractable. A complete, exact solution is developed in §2 and §3, taking the form of a sum of uncoupled, orthogonal normal modes plus a (near-field) branch line integral. (A full description of the field solely in terms of normal modes is impossible.) Although the modes (i.e. depth eigenfunctions) are given by a rather obscure special function (Macdonald's function of imaginary order, as in the kernel of the Kontorovich–Lebedev transform), which is slow to compute, it possesses an integral representation that lends itself to evaluation by asymptotic techniques. This results in an expression for the modes involving only elementary functions and an Airy function, thus providing a solution for the field which is easy to interpret physically, is quick to evaluate, and is essentially exact since in all cases of practical interest the asymptotic approximations are remarkably accurate. (In the case of the downward refracting profile the modes are all identically zero and the field is given by the branch line integral alone.)

The physical properties of the inverse-square modes, discussed in §4, turn out to be rather different from those of modes in a conventional waveguide. Each mode, for example, shows an oscillatory region immediately beneath the surface, terminating at the extinction depth, below which the mode becomes evanescent, decaying exponentially to zero; the extinction depth increases exponentially with mode number and with the reciprocal of the acoustic frequency; and, although each mode contains an evanescent region, there is no mode cut-off and there are no evanescent modes. All but one or two of the modes show the same distribution of zeros (nodes), which allows multimode suppression to be achieved by careful selection of the source and/or receiver depths.

To illustrate the nature of the modal propagation, the theory is applied in §5 to the problem of long-range acoustic transmission in the Arctic Ocean. The effects of multimode suppression are discussed in connection with VLF propagation, and the point spectrum is shown to rise rapidly between 5 and 50 Hz, by two to three orders of magnitude. This is associated with a reduction in the number of significant modes which occurs as the frequency falls, and is consistent with a deep minimum regularly observed around 5 Hz in Arctic Ocean ambient noise spectra. Dispersion and modal travel times are also considered in §5, in connection with an ocean-acoustic

PHILOSOPHICAL TRANSACTIONS OF THE ROYAL SOCIETY A MATHEMATICAL, PHYSICAL & ENGINEERING SCIENCES

tomography experiment that has recently been conducted under partial ice cover in the Greenland Sea.

A detailed comparison is made in §6 between the inverse-square theory and the results of an elegant experiment conducted in the ocean by Farmer & Vagle (1989). With a hydrophone close to the surface, in the vicinity of the surface bubble layer, they recorded the sounds of individual wave-breaking events at two different sites, identified as La Perouse and FASINEX. In both cases the near-surface (first 10 m) sound speed profiles were also measured and shown to be upward refracting, due to entrained bubbles, with the surface channel at FASINEX being notably deeper than that at La Perouse.

The spectrum of each wave-breaking event from La Perouse shows well-defined peaks in the measurement band 3–20 kHz, whilst the FASINEX data are qualitatively different, showing broad spectral bands, separated by fairly well-defined nulls. By fitting the inverse-square profile to each of the measured profiles, the spectral features in the two data-sets are reproduced accurately and in detail by the theory, confirming that the spectral phenomena are indeed an effect of the propagation conditions in the bubble layer. Moreover, the banding observed in the FASINEX spectra is interpreted as a modulation phenomenon, which is controlled by the depth of the source.

From the spectral width of the measured modulation peaks, the inverse-square theory provides an estimate of the depth of the acoustic sources associated with wave-breaking, that is to say, the depth of the acoustically active bubbles. According to the theory, the sources in FASINEX were 1.5 m below the surface, a position which coincides approximately with the base of the bubble clouds. Most of the constituents of the bubble layer are expected to be quiescent, since bubbles are effective acoustic radiators only during the first few milliseconds of their existence (Medwin & Beaky 1989). At present it is not clear why the noisy bubbles, constituting a small fraction of the total population, should lie at or close to the base of the bubble layer. This remains an open question, but one that needs to be resolved if reliable estimates of gas fluxes across the air–sea interface are to be achieved from acoustic observations of wave breaking.

2. Theory: propagation in an inverse-square profile

Consider a point, impulsive source of strength Q located at depth z' (measured from the origin of z) in a semi-infinite ocean with an inverse-square profile. The (time-dependent) velocity potential of the field, $g(t)$, satisfies both the inhomogeneous wave equation and the pressure-release boundary condition at the surface $z = z_s$. The Fourier transform of $g(t)$ with respect to time is the (complex) harmonic velocity potential, $G(\mathrm{j}\omega)$ where $\mathrm{j} = \sqrt{-1}$ and ω is angular frequency. The harmonic velocity potential satisfies the Fourier transformed (with respect to time) wave equation, that is to say, the Helmholtz equation:

$$\nabla^2 G + [\omega^2/c^2(z)]\, G = -Q\delta(\boldsymbol{r} - \boldsymbol{r}'), \tag{3}$$

where ∇^2 is the laplacian, $\delta(\cdot)$ is the Dirac delta function, and $\boldsymbol{r}, \boldsymbol{r}'$ are the coordinates of the receiver and source, respectively. With $c(z)$ representing the inverse-square sound-speed profile, as defined in (1), the (unique) solution of (3) is sought that satisfies the pressure-release boundary condition at the surface:

$$G = 0 \quad \text{at} \quad z = z_s. \tag{4}$$

A cylindrical coordinate system with the z-axis vertical and passing through the source point is the appropriate choice for a horizontally isotropic medium of uniform depth (which is our case). In view of the azimuthal uniformity of the field, the Helmholtz equation in this coordinate system takes the two-dimensional form

$$\frac{1}{r}\frac{\partial}{\partial r}\left(r\frac{\partial G}{\partial r}\right)+\frac{\partial^2 G}{\partial z^2}+\frac{\omega^2}{c^2(z)}G=-\frac{Q}{\pi r}\delta(r)\,\delta(z-z'), \tag{5}$$

where z, z' are, respectively, the receiver and source depths measured from the origin, and r is the horizontal range from the source to the receiver. The first step in the solution for G is to apply to (5) a zero-order Hankel transform with respect to range. This transform is defined as

$$G_p=\int_0^\infty rGJ_0(pr)\,\mathrm{d}r \tag{6a}$$

and the inverse transform is

$$G=\int_0^\infty pG_pJ_0(pr)\,\mathrm{d}r, \tag{6b}$$

where $J_0(pr)$ is the zero order Bessel function of the first kind. The transform variable p in these expressions is in effect the horizontal wavenumber. The Hankel transformation of the second derivative with respect to range in (5) is (Papoulis 1968)

$$\int_0^\infty r\left\{\frac{1}{r}\frac{\partial}{\partial r}\left(r\frac{\partial G}{\partial r}\right)\right\}J_0(pr)\,\mathrm{d}r=-p^2G_p. \tag{7}$$

It follows that the Hankel transformation over range reduces the Helmholtz equation to an ordinary differential equation in z:

$$\frac{\partial^2 G_p}{\partial z^2}+\left\{\frac{\omega^2}{c^2(z)}-p^2\right\}G_p=-\frac{Q}{2\pi}\delta(z-z'). \tag{8}$$

By making a familiar change of field variable, to $U_p(z)$, defined through

$$G_p(z)=z^{\frac{1}{2}}U_p(z), \tag{9}$$

the differential equation in (8) takes the form

$$\frac{1}{z}\frac{\partial}{\partial z}\left(z\frac{\partial U_p}{\partial z}\right)-\frac{U_p}{4z^2}+\left\{\frac{\omega^2}{c^2(z)}-p^2\right\}U_p=-\frac{Q}{2\pi z^{\frac{1}{2}}}\delta(z-z'). \tag{10}$$

This reduces to an inhomogeneous form of Bessel's equation when $c(z)$ is replaced by the expression for the inverse-square profile in (1):

$$\frac{1}{z}\frac{\partial}{\partial z}\left(z\frac{\partial U_p}{\partial z}\right)+\left\{\eta^2-\frac{\mu^2}{z^2}\right\}U_p=-\frac{Q}{2\pi z^{\frac{1}{2}}}\delta(z-z'), \tag{11}$$

where

$$\eta=\sqrt{(k_\infty^2-p^2)}, \tag{12}$$

$$\mu=\sqrt{(\tfrac{1}{4}-k_\infty^2 z_1^2)}, \tag{13}$$

and

$$k_\infty=\omega/c_\infty. \tag{14}$$

For a lossless medium k_∞ is real and η, μ are either real or imaginary (but not complex). In particular, μ is real for a (lossless) downward refracting medium,

whereas in the upward refracting case, for 'high' frequencies such that $k_\infty z_1 > \frac{1}{2}$, μ is imaginary.

Bessel's (inhomogeneous) equation can be solved quite naturally using the familiar properties of Hankel transforms. Since the z-domain in the ocean extends from a finite value ($z = z_s$) at the surface, rather than zero, it is necessary to use a *finite* Hankel transform, as discussed by Sneddon (1945, 1946), the appropriate form being

$$U_{p,s} = \int_{z_s}^{\infty} z U_p(z)\, J_\mu(sz)\, \mathrm{d}z, \tag{15}$$

where $J_\mu(sz)$ is a Bessel function of the first kind of order μ. The corresponding inverse transform is

$$U_p = \int_0^{\infty} s U_{p,s}\, J_\mu(sz)\, \mathrm{d}s. \tag{16}$$

(Finite Hankel transforms have recently been used by Buckingham (1988) in the analysis of a field problem with spherical symmetry.) When the transform of order μ in (15) is applied to the differential operator on the left of (12), the result is

$$\int_{z_s}^{\infty} z \left\{ \frac{1}{z}\frac{\partial}{\partial z}\left(z\frac{\partial U_p}{\partial z}\right) - \frac{\mu^2}{z^2} \right\} J_\mu(sz)\, \mathrm{d}z = -s^2 U_{p,s} + z_s U_p(z_s)\, J'_\mu(sz_s) - z_s J_\mu(sz_s)\, U'_p(z_s), \tag{17}$$

where the primes denote differentiation with respect to z. Thus, the boundary conditions (field and field-gradient) at the surface are included explicitly in this formalism through the last two terms on the right of (17). Since the surface is a pressure-release boundary, the field term, $U_p(z_s)$, is identically zero, and hence the second term on the right of (17) vanishes, whereas the field gradient, $U'_p(z_s)$, in the final term is an unknown quantity to be determined shortly.

On applying the Hankel transform in (15) to the differential equation (11), an algebraic equation is obtained whose solution is

$$U_{p,s} = [(Q/2\pi)\, z'^{\frac{1}{2}} J_\mu(sz') - z_s J_\mu(sz_s)\, U'_p(z_s)]/(s^2 - \eta^2). \tag{18}$$

The inverse transform of $U_{p,s}$, according to (16), is

$$U_p = \frac{Qz'^{\frac{1}{2}}}{2\pi} \int_0^{\infty} \frac{s J_\mu(sz')\, J_\mu(sz)}{(s^2 - \eta^2)}\, \mathrm{d}s - z_s U'_p(z_s) \int_0^{\infty} \frac{s J_\mu(sz_s)\, J_\mu(sz)}{(s^2 - \eta^2)}\, \mathrm{d}s, \tag{19}$$

and, as the integrals here are known forms (Watson 1958), the solution can be written explicitly:

$$U_p = \frac{\mathrm{j}\pi}{2}\left[\frac{Qz'^{\frac{1}{2}}}{2\pi} J_\mu(\eta z)\, H^{(1)}_\mu(\eta z') - z_s U'_p(z_s)\, J_\mu(\eta z_s)\, H^{(1)}_\mu(\eta z) \right], \quad z \leqslant z', \tag{20}$$

where $H^{(1)}_\mu(\,)$ is a Hankel function of the first kind of order μ. (When $z > z'$ the result is as in (20) except that z and z' are interchanged in the first product of Bessel and Hankel functions on the right.)

To determine the unknown factor $U'_p(z_s)$, representing the gradient of U_p at the surface, (20) is differentiated with respect to z and the result evaluated at $z = z_s$. Some simple algebra then leads to the expression

$$U'_p(z_s) = \frac{Qz'^{\frac{1}{2}}}{2\pi z_s} \frac{H^{(1)}_\mu(\eta z')}{H^{(1)}_\mu(\eta z_s)}, \tag{21}$$

where we have used the wronskian (Arfken 1966)

$$J_\mu(\eta z_s)\,H_\mu^{(1)\prime}(\eta z_s) - J_\mu'(\eta z_s)\,H_\mu^{(1)}(\eta z_s) = 2\mathrm{j}/\pi z_s. \tag{22}$$

From (20), (21) and (9), the solution for the Hankel-transformed harmonic velocity potential, G_p, is

$$\begin{aligned} G_p &= z^{\frac{1}{2}} U_p \\ &= \tfrac{1}{4}\mathrm{j}Q\sqrt{(zz')}\,\frac{H_\mu^{(1)}(\eta z')}{H_\mu^{(1)}(\eta z_s)}\,[J_\mu(\eta z)\,H_\mu^{(1)}(\eta z_s) - J_\mu(\eta z_s)\,H_\mu^{(1)}(\eta z)]. \end{aligned} \tag{23}$$

This result holds for $z \leqslant z'$, i.e. when the receiver is shallower than the source; when $z > z'$, the same result holds but with z and z' interchanged. The final step in obtaining the formal solution for the harmonic velocity potential G is to take the inverse transform of G_p, as defined by (6*b*), which yields

$$G = \tfrac{1}{8}\mathrm{j}Q\sqrt{(zz')}\int_0^\infty p\,\frac{H_\mu^{(1)}(\eta z')}{H_\mu^{(1)}(\eta z_s)}\,[H_\mu^{(2)}(\eta z)\,H_\mu^{(1)}(\eta z_s) - H_\mu^{(2)}(\eta z_s)\,H_\mu^{(1)}(\eta z)]\,J_0(pr)\,\mathrm{d}p,$$

$$\text{for} \quad z \leqslant z' \tag{24a}$$

and

$$G = \tfrac{1}{8}\mathrm{j}Q\sqrt{(zz')}\int_0^\infty p\,\frac{H_\mu^{(1)}(\eta z)}{H_\mu^{(1)}(\eta z_s)}\,[H_\mu^{(2)}(\eta z')\,H_\mu^{(1)}(\eta z_s) - H_\mu^{(2)}(\eta z_s)\,H_\mu^{(1)}(\eta z')]\,J_0(pr)\,\mathrm{d}p,$$

$$\text{for} \quad z > z' \tag{24b}$$

where the Bessel functions of order μ have been replaced by a sum of Hankel functions of the first and second kind.

The expressions in (24) represent a complete, exact solution for the harmonic velocity potential from a point source in a semi-infinite ocean with an inverse-square sound speed profile. Clearly, the solution satisfies the pressure-release boundary condition at the surface, for when z equals z_s (i.e. the receiver is on the surface) the integrand in (24*a*) is identically zero; and it also satisfies reciprocity since G is invariant under an exchange of source/receiver coordinates.

As a check on the formulation in (24), consider the case of an isovelocity profile ($z_1 = 0$). According to (13), the parameter μ, which appears as the order of the Hankel functions in the integrands of (24), is then equal to $\frac{1}{2}$. In general, Bessel functions of half-odd-integer order can be represented exactly by elementary functions, the appropriate forms in the present case being as follows (Lebedev 1965):

$$H_{\frac{1}{2}}^{(1)}(\alpha) = -\mathrm{j}[2/\pi\alpha]^{\frac{1}{2}}\exp(\mathrm{j}\alpha); \quad H_{\frac{1}{2}}^{(2)}(\alpha) = \mathrm{j}[2/\pi\alpha]^{\frac{1}{2}}\exp(-\mathrm{j}\alpha). \tag{25}$$

With these expressions, (24*a*) and (24*b*) both reduce to the same integral, which is a known form (Erdélyi 1954):

$$\begin{aligned} G_{iso} &= \tfrac{1}{4}\mathrm{j}Q\int_0^\infty p\,\frac{\exp\{\mathrm{j}\eta|z-z'|\} - \exp\{\mathrm{j}\eta(z+z'-2z_s)\}}{\eta}\,J_0(pr)\,\mathrm{d}p \\ &= (Q/4\pi R_1)\exp(\mathrm{j}k_\infty R_1) - (Q/4\pi R_2)\exp(\mathrm{j}k_\infty R_2), \end{aligned} \tag{26}$$

where

$$R_1 = \sqrt{[(z-z')^2 + r^2]}, \quad R_2 = \sqrt{[(z+z'-2z_s)^2 + r^2]} \tag{27}$$

are, respectively, the distances from the receiver to the source and to the negative image of the source formed by the pressure-release surface. Equation (26), which is

clearly correct, is the Lloyd's mirror solution for the field from a point source in a semi-infinite, isospeed medium with a pressure-release boundary.

Although (24) provide a general solution for the field, the integrals are awkward to evaluate either by approximate analytical techniques or, because of the particular special functions in each integrand, by numerical integration schemes. A further criticism that might be levelled at the formalism is that it provides little insight into the physical properties, particularly the modal structure, of the sound field in the inverse-square profile. Fortunately, it is possible to express the solution in an alternative form that is easier to interpret and evaluate. A procedure for making the conversion, which relies on arguments involving the deformation of the path of integration in the complex p-plane, is described in the following section.

3. Discrete and continuous components of the field

In the present discussion it is necessary to consider only one of the expressions in (24), since the same argument applies to both but with z and z' interchanged. Taking the case where $z' \geqslant z \geqslant z_s$, the first step is to represent the Bessel function in the integrand as the sum of two zero-order Hankel functions, allowing the field to be expressed as the sum of two integrals, I_1 and I_2:

$$G = \tfrac{1}{16}\mathrm{j}\, Q\sqrt{(zz')}\,\{I_1 + I_2\}, \tag{28}$$

where

$$I_1 = \int_0^\infty pS_\mu(\eta)\, H_0^{(1)}(pr)\,\mathrm{d}p, \tag{29a}$$

$$I_2 = \int_0^\infty pS_\mu(\eta)\, H_0^{(2)}(pr)\,\mathrm{d}p, \tag{29b}$$

and

$$S_\mu(\eta) = \frac{H_\mu^{(1)}(\eta z')}{H_\mu^{(1)}(\eta z_s)}[H_\mu^{(2)}(\eta z)\, H_\mu^{(1)}(\eta z_s) - H_\mu^{(1)}(\eta z)\, H_\mu^{(2)}(\eta z_s)], \quad \text{for} \quad z' > z. \tag{30}$$

The procedure for manipulating I_1 and I_2 in the complex p-plane is only briefly described below, with the details relegated to Appendix A.

Since the radical η, defined in (12), has branch points at $p = \pm k_\infty$, it is implicit that two branch cuts must be made in the p-plane. These cut lines are chosen in such a way that $\mathrm{Im}\,(\eta) > 0$ over the top Riemann sheet, to ensure that $S_\mu(\eta)$ converges to finite values everywhere on the sheet. By making appropriate substitutions, the pair of integrals in (29) are combined into a single-line integral on the sheet, and the integration path is then deformed to follow the cut lines.

In deforming the path of integration, the (simple) poles of $S_\mu(\eta)$, corresponding to the zeros of the Hankel function in the denominator of (30), are enclosed by the contour. It follows that the final form of the field solution consists of two components: a branch line integral (continuous field), which decays relatively rapidly with range, and an infinite sum of normal modes (discrete field), corresponding to the residues of the poles enclosed by the integration contour.

From Appendix A the final version of the general solution for the field in the inverse-square profile is

$$G = G_{\mathrm{bl}} + G_{\mathrm{nm}}, \tag{31a}$$

where

$$G_{\mathrm{bl}} = \tfrac{1}{16}\mathrm{j}Q\sqrt{(zz')}\int_{-\infty}^{\infty} \eta S_\mu(\eta)\, H_0^{(1)}(\sqrt{(k_\infty^2 - \eta^2)}\, r)\,\mathrm{d}\eta \tag{31b}$$

PHILOSOPHICAL TRANSACTIONS OF THE ROYAL SOCIETY A MATHEMATICAL, PHYSICAL & ENGINEERING SCIENCES

is the branch line integral and

$$G_{\mathrm{nm}} = -\tfrac{1}{8}\pi Q \sqrt{(zz')} \sum_{m=1}^{\infty} \frac{\eta_m H_\mu^{(2)}(\eta_m z_{\mathrm{s}}) H_\mu^{(1)}(\eta_m z) H_\mu^{(1)}(\eta_m z')}{\partial H_\mu^{(1)}(\eta z_{\mathrm{s}})/\partial \eta |_{\eta=\eta_m}} H_0^{(1)}(\sqrt{(k_\infty^2 - \eta_m^2)}\, r) \quad (31c)$$

is the sum of normal modes. The roots of the characteristic equation

$$H_\mu^{(1)}(\eta z_{\mathrm{s}}) = 0 \quad (32)$$

give the eigenvalues η_m for modes $m = 1, 2, 3, \ldots$. The properties of the Hankel functions, $H_\mu^{(1)}(\eta_m z)$, representing the modes, the roots of (32), and the behaviour of the mode sum are examined below in §4.

There are no approximations in the analysis leading to (31), which, like the original formulation in (26), constitute an exact solution for the field. But the new expressions provide a better physical picture of the field through the explicit appearance of the normal modes. Moreover, the zeros of the Hankel function in (32), which are required to specify the eigenvalues, can be accurately determined using asymptotic techniques.

There are two situations in which the modal sum, G_{nm}, vanishes and the field consists solely of the branch line integral, G_{bl}: the first is when μ is real, which includes the isospeed profile (i.e. $z_1 = 0$) and all downward-refracting inverse-square profiles (i.e. z_1 imaginary); and the second is when $z_{\mathrm{s}} = 0$, a condition implying an upward-refracting inverse-square profile (i.e. z_1 real), with the sound speed at the sea surface equal to zero. Under the first condition, in which the order μ is real, the Hankel function in (32) has no zeros (Watson 1958), hence there are no poles in the complex p-plane, which in turn means there are no residues and thus no normal modes. The second case, in which $z_{\mathrm{s}} = 0$, is something of a curiosity. From the identity (Abramowitz & Stegun 1965)

$$\lim_{z_{\mathrm{s}} \to 0} \frac{H_\mu^{(2)}(\eta z_{\mathrm{s}})}{H_\mu^{(1)}(\eta z_{\mathrm{s}})} = -1, \quad (33)$$

it follows that there are no poles in $S_\mu(\eta)$, and thus no normal modes. Physically, the absence of modes occurs, even though the profile is upward refracting, because the phase velocity falls to zero on the surface, making it effectively anechoic: sound propagating towards the surface eventually slows to a halt, its kinetic energy having been converted to potential energy, leaving the medium, in the absence of internal losses, permanently strained. Thus, there is no prospect of a reflected wave propagating away from the surface into the region of finite sound speed. Since the existence of modes requires multiple reflections from the boundary, the modal contribution is identically zero. A fuller account of the branch line integral and the properties of the field when $z_{\mathrm{s}} = 0$ is given by Buckingham (1990*a*). The discussion hereafter addresses only the modal component of the field, which in most situations of interest is dominant.

4. The modal field

As we have seen, and assuming now that $z_{\mathrm{s}} > 0$, normal modes exist in the inverse-square profile when μ is imaginary, or equivalently when $k_\infty z_1 > \frac{1}{2}$. When this condition holds it is convenient to work with the real variable

$$\nu \equiv \mathrm{j}\mu = \sqrt{(k_\infty^2 z_1^2 - \tfrac{1}{4})} \geqslant 0. \quad (34)$$

With this definition, (32) must be solved for the eigenvalues.

The zeros of Hankel functions have often featured in radiation problems, dating back to the early work of Watson (1918, 1919) on diffraction of electromagnetic waves by the earth. They are also important in quantum mechanical scattering problems (Regge 1959) showing spherical or cylindrical symmetry. These and other applications have stimulated a number of investigations of the zeros, notably by Magnus & Kotin (1960), with refinements and extensions added by Keller *et al.* (1963) and Cochran (1965).

The analyses show that the only roots of the Hankel function of the first kind of imaginary order are themselves imaginary. Thus, to specify the modes and, in particular, to find the roots of the characteristic equation it is necessary to establish the properties of the special function $H^{(1)}_{-\mathrm{j}\nu}(\mathrm{j}\sigma)$, where σ and ν are real and positive. It turns out, as shown below, that the function $H^{(1)}_{-\mathrm{j}\nu}(\mathrm{j}\sigma)$ (or equivalently, Macdonald's function $K_{\mathrm{j}\nu}(\sigma)$) has a relatively simple asymptotic representation, from which all the characteristics of the modes are readily deduced. The properties of the Hankel function of the second kind, $H^{(2)}_{-\mathrm{j}\nu}(\mathrm{j}\sigma)$, which also appears in the mode sum, as part of the mode coefficient, are also developed below.

4.1. *The Hankel function* $H^{(1)}_{-j\nu}(j\sigma)$

A straightforward argument is given in Appendix B which leads to the integral representation

$$\begin{aligned} U_\nu(\sigma) &\equiv \mathrm{j}\,\mathrm{e}^{\nu\pi} H^{(1)}_{-\mathrm{j}\nu}(\mathrm{j}\sigma) \\ &= \frac{1}{\pi}\int_{-\infty}^{\infty} \exp\{\mathrm{j}\nu[u-\sigma/\nu\sinh(u)]\}\,\mathrm{d}u, \end{aligned} \tag{35}$$

where the normalization ensures that the amplitude of the (real) function $U_\nu(\sigma)$ is not excessively small when $\nu \gg 1$. Figure 2*a* and *b* shows the 'exact' form of the normalized function for $\nu = 10$ and $\nu = 2$, respectively, computed using a Simpson's rule algorithm to evaluate the integral. It is noteworthy that, as the scaling of the σ axis is logarithmic, the constant period and amplitude in the oscillatory region, where $\sigma < \nu$, indicates that $U_\nu(\sigma)$ shows a $\cos(\ln(\sigma))$ dependence. As σ increases through ν, the function shows a slight rise in amplitude and then becomes evanescent, decaying exponentially to zero. The *extinction* point, where the oscillatory behaviour ceases and the function begins its exponential decay, is defined by equality of the magnitudes of the order and argument, i.e. by $\sigma = \nu$. ('Extinction' rather than 'cut-off' is used for the termination of the oscillatory region, since the latter term has other connotations in connection with waveguide propagation. Specifically, mode cut-off occurs when the horizontal wavenumber switches from real to imaginary, a transition which does not occur in the inverse-square profile.)

The integral in (35) is slow to compute and cannot be solved easily for the eigenvalues. Both difficulties are eliminated by turning to asymptotics (Appendix B). For $\nu > \sigma$ (oscillatory region), a standard application of first-order stationary phase theory yields the expression

$$U_\nu(\sigma) \approx -\frac{2}{\pi}\frac{\sqrt{(2\pi)}}{(\nu^2-\sigma^2)^{\frac{1}{4}}}\cos\left\{\nu\ln\left[\frac{\nu+\sqrt{(\nu^2-\sigma^2)}}{\sigma}\right]-\sqrt{(\nu^2-\sigma^2)}-\tfrac{1}{4}\pi\right\}, \tag{36a}$$

(notice the cosine of the logarithm); and a second-order analysis gives

$$U_\nu(\sigma) \approx -2(2/\sigma)^{\frac{1}{3}}\,\mathrm{Ai}[(2/\sigma)^{\frac{1}{3}}(\sigma-\nu)], \tag{36b}$$

PHILOSOPHICAL TRANSACTIONS OF THE ROYAL SOCIETY A MATHEMATICAL, PHYSICAL & ENGINEERING SCIENCES

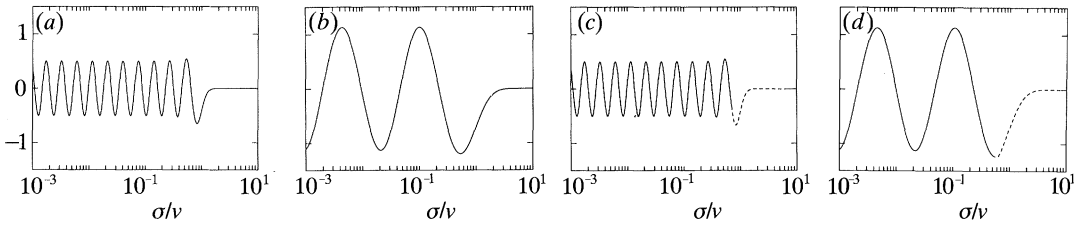

Figure 2. The normalized function $U_\nu(\sigma)$ evaluated as follows: (*a*) and (*b*) from the integral in (35) using Simpson's rule; and (*c*) and (*d*) from the matched asymptotic expressions in (36*a*) (solid line) and (36*b*) (dashed line). (*a*) $\nu = 10$; (*b*) $\nu = 2$; (*c*) $\nu = 10$; (*d*) $\nu = 2$.

which, through the Airy function of the first kind, Ai[ ], describes the decay of the Hankel function as it passes through the extinction point into evanescence. The two asymptotic forms in (36) are matched in the oscillatory region somewhere close to the extinction point. (The precise position of the matching point is generally not critical, except perhaps when ν is close to zero, in which case some care needs to be exercised.) Equations (36) are plotted in figure 2*c* and *d* for $\nu = 10$ and $\nu = 2$, respectively. A comparison with the exact forms in figure 2*a* and *b* reveals the remarkable precision of the matched asymptotic approximations. Even for small values of ν, of order unity, representing an extreme low-frequency condition in which the profile is about to cease supporting normal modes, the matched asymptotic expressions are essentially exact.

The zeros of the Hankel function can now be determined directly from (36*a*), since they occur when the argument of the cosine function is an odd multiple of $\frac{1}{2}\pi$. Thus, the mth zero, $\sigma = \sigma_m$, is the solution of the transcendental equation

$$\nu \ln\left[(\nu + \sqrt{(\nu^2 - \sigma_m^2)})/\sigma_m\right] - \sqrt{(\nu^2 - \sigma_m^2)} - \tfrac{1}{4}\pi = \tfrac{1}{2}(2m-1)\,\pi, \quad m = 1, 2, \ldots . \tag{37}$$

For ν somewhat larger than σ_m, a good approximate solution of (37) is obtained by neglecting σ_m in both radicals. This yields the result

$$\sigma_m \approx 2\nu \exp\left(\pi/4\nu - m\pi/\nu - 1\right), \tag{38}$$

showing that σ_m decays exponentially with mode number.

The 'exact' zeros of $H^{(1)}_{-\mathrm{j}\nu}(\mathrm{j}\sigma)$ may now be calculated from (37) by using Newton's iterative root-finding formula, taking the approximation in (38) as the starting value. Table 1 shows the first ten zeros calculated in this way and, for comparison, the approximate values from (38). Although there is reasonable agreement, improving as m increases, the approximate zeros are consistently too low, a discrepancy that would lead to a violation of the pressure-release boundary condition if the approximate values were used to characterize the modes. It is therefore important to solve (37) 'exactly' for σ_m, a procedure which requires negligible computational effort, typically involving no more than five iterations to achieve convergence.

At low frequencies, corresponding to small values of ν, a small mismatch between the asymptotic forms in (36) may occur if the matching point is not chosen carefully. This is a minor problem, but nevertheless one that may be avoided, once the eigenvalues have been determined from (37), by using as an alternative to (36) a uniform asymptotic approximation derived from Langer's (1932, 1949) turning point theory (Balogh 1967; Olver 1974):

$$U_\nu(\sigma) \approx -2\sqrt{2}\,\nu^{\frac{1}{6}}(\Omega/(\nu^2 - \sigma^2))^{\frac{1}{4}}\,\mathrm{Ai}\,(-\nu^{\frac{2}{3}}\Omega), \tag{39a}$$

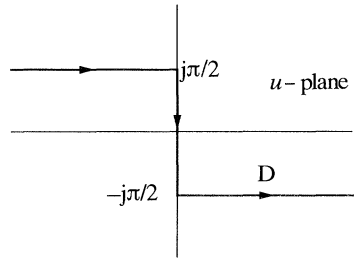

Figure 3. Path of integration D in the complex u-plane.

Table 1. *Zeros of* $H^{(1)}_{-j\nu}(j\sigma)$ *for* $\nu = 10$ *from (37) (exact) and (38) (approximate)*

m	σ_m (exact)	σ_m (approx.)
1	6.5043	5.8131
2	4.4693	4.2459
3	3.1818	3.1012
4	2.2954	2.2651
5	1.6660	1.6545
6	1.2129	1.2084
7	0.8844	0.8826
8	0.6454	0.6447
9	0.4711	0.4709
10	0.3440	0.3439

where
$$\Omega = \left\{\frac{3}{2}\left[\ln\left(\frac{\nu+\sqrt{(\nu^2-\sigma^2)}}{\sigma}\right)-\frac{\sqrt{(\nu^2-\sigma^2)}}{\nu}\right]\right\}^{\frac{2}{3}}. \tag{39b}$$

Although valid for all σ on both sides of the extinction point, (39a) is slower to compute than the matched asymptotics, through the presence of the Airy function over the full range of σ.

Some elementary algebra applied to the first-order approximation in (36a) yields the expression
$$\left.\frac{\partial U_\nu}{\partial\sigma}\right|_{\sigma=\sigma_m} \approx (-1)^m 2\sqrt{\left(\frac{2}{\pi}\right)}\frac{(\nu^2-\sigma_m^2)^{\frac{1}{4}}}{\sigma_m}. \tag{40}$$

This result will be used later in the denominator of the coefficient in the mode sum.

4.2. *The Hankel function* $H^{(2)}_{-j(\nu)}(j\sigma)$

The coefficient in the mode sum also contains the Hankel function of the second kind of imaginary order. For reasons to do with convergence, it is not possible to express $H^{(2)}_{-j(\nu)}(j\sigma)$ (σ real and positive) as an integral along the real axis between $\pm\infty$ but it can be represented as the contour integral (Lebedev 1965)
$$e^{-\nu\pi}H^{(2)}_{-j(\nu)}(j\sigma) = -\frac{1}{j\pi}\int_D \exp\{j\nu u+\sigma\cosh u\}\,du, \tag{41}$$

where the path of integration D is shown in figure 3. (The exponential normalization ensures that excessively large values are not encountered when $\nu \gg 1$.)

By examining the turning points of the exponent in the integrand, it may be shown

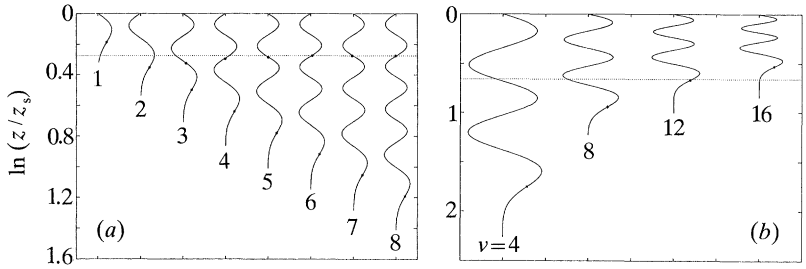

Figure 4. (*a*) Mode shapes 1–8 as a function of normalized depth for $\nu = 10$. (*b*) Mode 5 for four values of ν, indicating the effect of progressively increasing the frequency. See text for details of both diagrams.

that there is only one saddle point on the contour, on the path to the right of the imaginary axis. A straightforward steepest-descent analysis yields

$$\begin{aligned} \mathrm{e}^{-\nu\pi} H^{(2)}_{-\mathrm{j}(\nu)}(\mathrm{j}\sigma_m) &\approx -\frac{1}{j\pi}\frac{\sqrt{(2\pi)}}{(\nu^2-\sigma_m^2)^{\frac{1}{4}}} \\ &\quad \times \exp j\left\{\nu \ln\left[\frac{\nu+\sqrt{(\nu^2-\sigma_m^2)}}{\sigma_m}\right] - \sqrt{(\nu^2-\sigma_m^2)} - \tfrac{1}{4}\pi\right\} \\ &= (-1)^m \sqrt{(2/\pi)}\,(\nu^2-\sigma_m^2)^{-\frac{1}{4}}. \end{aligned} \tag{42}$$

The final expression here derives from (37) for σ_m. Obviously, since σ_m is always less than ν, the second-order asymptotic form is not required in this case. The accuracy of the approximation in (42) is comparable with that of the asymptotic expressions in the preceding section.

4.3. *Physical properties of the normal modes*

By setting

$$\eta_m = \mathrm{j}\,\sigma_m/z_\mathrm{s}, \tag{43}$$

where σ_m is the solution of (37), and defining $\zeta = z/z_\mathrm{s}$ as the depth (below the origin) normalized to the z-coordinate of the surface, the (normalized) mode functions can be written as $U_\nu(\sigma_m \zeta)$. These functions are orthogonal with weight ζ on the interval $[1, \infty]$ (i.e. over the water column), as may be proved using standard theory of orthogonal functions. They are given by either the matched or uniform asymptotic forms in (36) and (39), respectively; and, through the characteristic equation in (32), it is evident that they satisfy the pressure-release condition on the surface, where $\zeta = 1$.

Figure 4*a* shows the first eight (normalized) modes as a function of depth for $\nu = 10$. The mth mode shows m extrema, successive modes are opposite in sign immediately below the surface, and the amplitude of the oscillations shows a small increase just before extinction occurs. The extinction depth, ζ_ext, defined by the equality of argument and order, is

$$\zeta_\mathrm{ext} \equiv z_\mathrm{ext}/z_\mathrm{s} = \nu/\sigma_m \approx \tfrac{1}{2}\exp\{(m-\tfrac{1}{4})\,\pi/\nu + 1\}, \tag{44}$$

where the approximation follows from (38). Thus, as the mode number increases, the oscillatory part of the mode carrying the energy penetrates deeper into the ocean, as

illustrated in figure 4*a*. The asterisk at the base of the oscillatory region of each mode depicts the extinction depth; and as the asterisks are closely rectilinear, on a logarithmic depth scale, the dependence of the extinction depth on mode number is seen to be exponential, in accord with (44).

The zeros of the modes are distributed in such a way that multimode suppression may be achieved by selecting the depth of the source (receiver) appropriately. To illustrate the phenomenon, we refer again to figure 4*a*, where the black dots on modes 3–8 indicate the second zero measured down from the surface, and the horizontal dotted line signifies the depth of the source (receiver). For modes 5 and above the source (receiver) is at a null, so none of these modes is excited (detected). The same is true of mode 1, because it has passed into extinction. Mode 2, on the other hand, is strongly excited (detected), mode 3 moderately so and mode 4 only weakly. Thus, a source (receiver) at the depth of the second zero primarily excites (detects) the second mode, with small contributions also appearing from modes 3 and 4, while all remaining modes are nullified. This argument may be generalized to the qth zero and the qth mode; and from (36*a*), the depth z_q at which the source (receiver) should be located to select the qth mode is

$$z_q \approx z_s \exp(q\pi/\nu), \quad q = 1, 2, \ldots . \tag{45}$$

An example of multimode suppression is discussed in connection with sound transmission in the Arctic Ocean in §5.

As well as depending on mode number, the extinction depth varies with frequency, through the presence of ν in (44). Figure 4*b* illustrates the frequency dependence of mode 5. The extinction depth, depicted by the asterisk, rises with increasing frequency, effectively compressing the mode into a shallower region of the ocean. Thus, a receiver located at the depth of the horizontal dotted line detects the mode when $\nu = 4$ and $\nu = 8$; but when $\nu = 12$ the receiver coincides with the extinction depth, above which most of the energy in the mode is concentrated; and at higher values of ν the mode is no longer detectable, having passed into extinction. This is an example of *mode drop-out*, a phenomenon which will be re-examined in §6 on sound propagation in the surface bubble layer. The *extinction frequency* of a mode, defined as that frequency at which the extinction depth and the receiver depth are coincident, occurring when $\nu = 12$ in the example of figure 4*b*, is given by the expression

$$f_{\mathrm{ext}} = (c_\infty/2\pi z_1)\sqrt{(\nu_{\mathrm{ext}}^2 + \tfrac{1}{4})}, \tag{46a}$$

where, from (37) and (44),

$$\nu_{\mathrm{ext}} = (m - \tfrac{1}{4})\pi\zeta/\{\zeta \ln(\zeta + \sqrt{(\zeta^2 - 1)}) - \sqrt{(\zeta^2 - 1)}\}. \tag{46b}$$

Alternatively, we may refer to f_{ext} as the drop-out frequency of the mode.

4.4. *The mode sum*

With a little algebra applied to the results of the preceding subsections, the sum of normal modes in (31*c*) can now be reduced to the following form:

$$G_{\mathrm{nm}} = -\frac{\pi Q\sqrt{(zz')}}{16 z_s^2} \sum_{m=1}^{\infty} \frac{\sigma_m^2}{\sqrt{(\nu^2 - \sigma_m^2)}} U_\nu(\sigma_m \zeta)\, U_\nu(\sigma_m \zeta')\, H_0^{(1)}\left(\sqrt{(k_\infty^2 z_s^2 + \sigma_m^2)}\,\frac{r}{z_s}\right), \tag{47}$$

where the mode functions, $U_\nu(\,)$, are expressed with precision by either the matched or uniform asymptotic forms in (36) and (39), respectively. The eigenvalues, σ_m,

are the solutions of (37). (Notice that the exponential normalizing factors in the mode functions cancel out of the mode sum.)

In most acoustic transmission problems the range and frequency are such that the Hankel function of zero order can be accurately represented by its asymptotic form:

$$H_0^{(1)}(p_m r) \approx \sqrt{(2/\pi p_m r)}\, \mathrm{e}^{-\mathrm{j}\pi/4} \exp(\mathrm{j} p_m r), \tag{48a}$$

where the familiar factor $r^{-\frac{1}{2}}$ is characteristic of cylindrical spreading. The horizontal wavenumber, p_m, is

$$p_m = \sqrt{(k_\infty^2 z_s^2 + \sigma_m^2)}/z_s, \tag{48b}$$

from which it follows that, as σ_m is real for all mode numbers, however high, p_m also is always real. Since the argument shows no transition from real to imaginary values, the Hankel function in (48*a*) is oscillatory for all the modes, that is to say there is no mode cut-off and there are no evanescent modes. (The evanescent region of each mode beneath the extinction depth should not be confused with an evanescent mode, which does not propagate in range.) The absence of mode cut-off in the inverse-square profile contrasts with the situation in say the Pekeris (1948) channel, where cut-off is a function of the channel depth and frequency. Cut-off also occurs in profiles showing a sharp discontinuity in gradient, as discussed by Labianca (1973) in connection with a bilinear refractive index profile. In the inverse-square profile, there is no physical constraint (boundary) to prevent the modes from extending indefinitely in depth, and hence no mechanism whereby mode cut-off could occur.

However, the modes do undergo attenuation with increasing mode number, although this is a relatively slow process compared with the abruptness of cut-off. The decay arises from the presence of the factor σ_m^2 in the numerator of the mode coefficient. In this context we define the *mode strength* as σ_m, which, according to (44), decays exponentially with mode number and enjoys a reciprocal relationship with the extinction depth:

$$\sigma_m \zeta_{\mathrm{ext}} = \nu. \tag{49}$$

In essence this states that shallow modes are strong, deep modes are weak. (N.B. The mode strength, σ_m, is distinct from the mode amplitude, the latter being the amplitude of the function $U_\nu(\sigma_m \zeta)$, which is usually of order unity.)

Given that the frequency, the source depth and receiver depth are fixed, there is a 'window' of modes, numbers M_1 up to M_2 say, which contribute significantly to the field. Those modes below M_1 are essentially zero, having passed into extinction, whereas above M_2 the modes are heavily attenuated by the square of the mode strength, σ_m^2, in the mode coefficient. An estimate of M_1 is found by setting $m = M_1$ in (44), to yield

$$M_1 \approx [\ln(2\zeta) - 1]\,\nu/\pi + \tfrac{1}{4} \quad \text{or} \quad M_1 = 1, \tag{50}$$

whichever is the greater. Taking as a measure of M_2 a reduction in the mode strength by a factor of e^{-1}, that is,

$$\sigma_{M_2}/\sigma_{M_1} \equiv \exp\{-(M_2 - M_1)\,\pi/\nu\} = \mathrm{e}^{-1}, \tag{51}$$

it follows that

$$M_2 \approx M_1 + \nu/\pi. \tag{52}$$

If ΔM, representing the number of significant modes is defined as the difference between M_2 and M_1, then

$$\Delta M \equiv (M_2 - M_1) \approx \nu/\pi \approx k_\infty z_1/\pi, \tag{53}$$

which indicates an approximately linear scaling of ΔM with both frequency and the profile parameter z_1. Notice that ΔM is independent of the receiver depth, even though the mean mode number

$$\langle M \rangle = \tfrac{1}{2}(M_1 + M_2) \tag{54}$$

increases with increasing z.

There is a similarity between (53) for ΔM and the expression for the total number of propagating modes, M_{total}, in a conventional isotropic waveguide with plane, parallel pressure-release boundaries of depth h:

$$M_{\text{total}} = kh/\pi, \tag{55}$$

where k is the wavenumber of the source radiation. In view of the analogy between the role of h in determining the number of propagating modes in the parallel-sided waveguide and that of z_1 in governing the number of significant modes in the inverse-square profile, the latter may be interpreted as the 'effective depth' of the inverse-square channel; that is to say, with $k = k_\infty$, a waveguide of depth $h = z_1$ supports the same number of modes as the inverse-square profile defined in (1). It is noteworthy that ΔM, the number of significant modes in the inverse-square profile, is independent of the position of the sea surface, z_s.

4.5. *Interference wavelength*

The oscillatory range dependence of the modes, represented by the Hankel function of zero order in (48a), implies that at any given frequency there is mutual interference between modes as they propagate away from the source. Modal interference imparts a complicated structure to the sound field, which increases in complexity as the frequency rises and more modes make a significant contribution to the mode sum. Similar behaviour is observed in a waveguide with fixed boundaries.

When only two modes contribute significantly to the mode sum, a series of interference peaks, regularly separated in range, feature prominently in the field. The interference wavelength, Δ_{mn}, between the peaks associated with a pair of modes, m and n, in an inverse-square profile is derived in the same way as for a conventional waveguide (Tolstoy & Clay 1966), yielding

$$\Delta_{\text{mn}} \approx 2\pi z_s / |\sqrt{(k_\infty^2 z_s^2 + \sigma_m^2)} - \sqrt{(k_\infty^2 z_s^2 + \sigma_n^2)}|. \tag{56}$$

This expression is used in §5.1.1 in the discussion of acoustic transmission in a typical Arctic Ocean profile.

It is implicit, when a simple regular structure of interference maxima is observed, that only a few significant modes are contributors to the field. In such circumstances, (56) is a useful diagnostic tool for identifying those modes that are present. On the other hand, in the presence of many significant modes (a situation commonly found in the ocean) the interference structure tends to be very complicated, in which case (56) loses its utility.

5. Arctic Ocean acoustics

In the ice-covered regions of the Arctic Ocean the sound speed shows a minimum of approximately 1440 m s^{-1} at the surface (Kuperman 1988), where the water is coldest, and a positive gradient which may persist down to depths of several thousand metres. Such a profile, in which the surface gradient is in the region of 0.05 s^{-1}, is very well represented by the upward-refracting (i.e. z_1 real) version of the inverse-square expression in (1). Figure 5 shows an inverse-square profile, with $z_1 =$

PHILOSOPHICAL TRANSACTIONS OF THE ROYAL SOCIETY A MATHEMATICAL, PHYSICAL & ENGINEERING SCIENCES

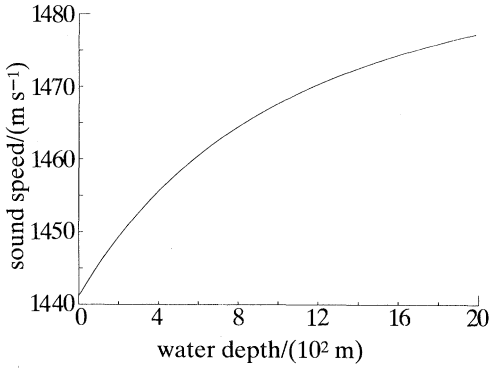

Figure 5. Inverse-square profile representative of Arctic waters ($z_s = 2000$ m, $z_1 = 525$ m, and $c_\infty = 1490$ m s^{-1}).

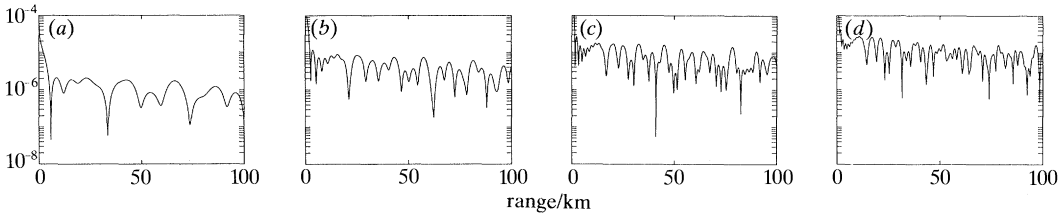

Figure 6. Range plots (Arctic) of $|G_{nm}|$ from (47) for the source and receiver at the same depth of 50 m ($Q = 1$). (*a*) $f = 10$ Hz; (*b*) $f = 20$ Hz; (*c*) $f = 30$ Hz; (*d*) $f = 40$ Hz.

525 m, $c_\infty = 1490$ m s^{-1} and $z_s = 2000$ m, that is fairly typical of Arctic conditions. At a frequency of 10 Hz the number of significant modes supported by this particular profile is $\Delta M \approx 7$; and at other frequencies ΔM is given by a simple linear scaling (e.g. at 40 Hz $\Delta M \approx 28$).

5.1. *VLF propagation*

In the infra-sonic frequency band (1–50 Hz) sound may propagate to long distances in the Arctic Ocean, as discussed by Milne (1967) on the basis of ray acoustics. Since ray theory is a doubtful approximation in the VLF band, a wave-theoretic approach to the problem is more appropriate at these frequencies. Attempts to compute the long-range acoustic field in the ocean using wave-theoretic numerical models date back to the early 1960s (Dorman 1962). More recent models include the fast field program (FFP) and SAFARI, developed, respectively, by Di Napoli (1971) and Schmidt & Glattetre (1985). In essence, both models compute the Green's function in an horizontally stratified medium. A multilayered representation is not an unreasonable approximation in a range-independent environment, and the FFP has been applied by Kutschale (1973) to the problem of propagation in the Arctic Ocean. Nevertheless, fast field programs, in common with most numerical propagation models, are computationally intensive.

By comparison, the inverse-square theory is quick and easy to evaluate. Figure 6 shows the magnitude of the modal field, $|G_{nm}|$, as a function of range, for frequencies 10, 20, 30 and 40 Hz. The curves were computed from (47) using the parameters of the Arctic profile given above, with source and receiver set at the same depth of 50 m below the surface. They show an average decay corresponding to cylindrical

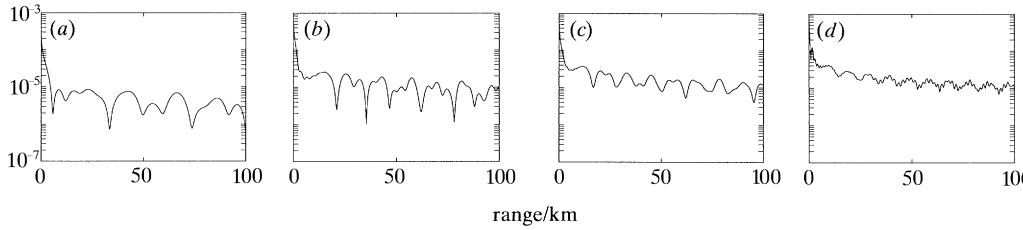

Figure 7. Range plots (Arctic) of $|G_{nm}|$ from (47) for source and receiver at the same depth of 112.4 m ($Q = 1$). Multimode suppression is evident in the curve for 30 Hz, as discussed in the text. (*a*) $f = 10$ Hz; (*b*) $f = 20$ Hz; (*c*) $f = 30$ Hz; (*d*) $f = 40$ Hz.

spreading (i.e. proportional to $r^{-\frac{1}{2}}$), superimposed upon which is a strong interference structure. The fluctuations increase in rapidity as the frequency rises, indicating the presence of an increasing number of significant modes in the field.

5.1.1. *Multimode suppression and mode interference*

Figure 7 shows similar range plots, for the same four frequencies, but with both the source and receiver at a depth (below the surface) of 112.4 m. This depth has been chosen advisedly to illustrate the phenomenon of multimode suppression, for at 30 Hz it coincides with the first zero in the higher-order modes. According to the argument in §4.3, we should expect the field at 30 Hz to be relatively smooth in this case, since it contains significant contributions only from the first three or four modes, with little or nothing coming from the higher-order modes (the number of significant modes is over 20). A comparison with the curve for 30 Hz in the previous figure confirms that multimode suppression does indeed have a significant effect on the field: the absence of the higher-order modes reduces the rate and amplitude of the fluctuations at the selected frequency. At the other three frequencies the full modal interference structure is retained.

Although the curves at 10 Hz vary more slowly than those at higher frequencies, they still show considerable complexity due to the presence of several modes ($\Delta M \approx 7$). At lower frequencies the situation is simpler, as illutrated in figure 8, which shows the magnitude of the velocity potential at a frequency of 2.5 Hz. The regular spacing of the interference maxima indicates that only two significant modes are present and, since the extinction depth of the first mode is approximately 2170 m (below the surface) at this frequency, lying well below the receiver, it may be anticipated that they are modes 1 and 2. This is confirmed by a calculation of the interference wavelength from (56), which yields $\Delta_{12} = 93.6$ m, closely matching the interval between the peaks in figure 8.

Another aspect of multimode suppression is illustrated in figure 9 showing the depth dependence of $|G_{nm}|$, for the profile in figure 5, at a range of 50 km from the source. As in figure 7 the source is at a depth of 112.4 m, which, at a frequency of 30 Hz, coincides with the first zero of the higher-order modes.

At the lower frequency of 20 Hz (figure 9*a*) the first four modes are prominent in the first 1200 m or so of the water column, at which depth mode four goes into extinction. Below 1200 m the contribution from individual modes is less recognizable but nevertheless the higher-order modes are present, as indicated by the more or less uniform sound spectral level down to 4000 m and beyond.

At 30 Hz (figure 9*b*), the first four modes are even more strongly in evidence, in this case at depths above 800 m, which is the extinction depth of mode four. The sound

PHILOSOPHICAL TRANSACTIONS OF THE ROYAL SOCIETY A MATHEMATICAL, PHYSICAL & ENGINEERING SCIENCES

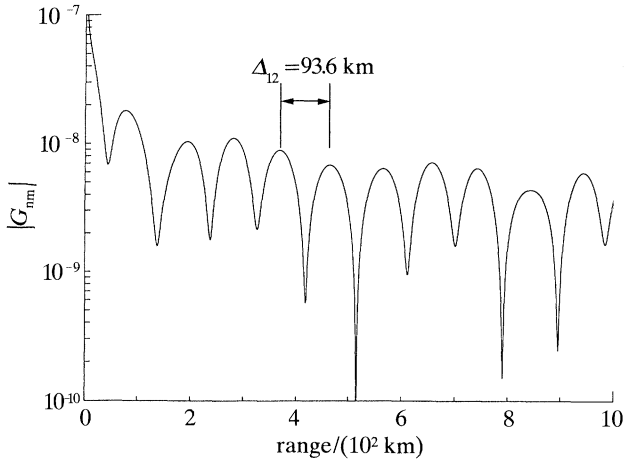

Figure 8. Range plot (Arctic) of $|G_{nm}|$ from (47) for the source and receiver at the same depth of 50 m ($Q = 1$). $f = 2.5$ Hz.

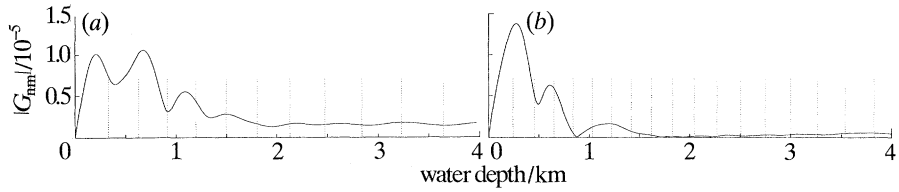

Figure 9. $|G_{nm}|$ (Arctic) as a function of depth at a range of 50 km, from (47) ($Q = 1$). The source depth is 112.4 m. The vertical dotted lines depict the extinction depths of successive modes, starting with mode 1 at the extreme left. (*a*) $f = 20$ Hz; (*b*) $f = 30$ Hz.

field is heavily attenuated at greater depths, most noticeably below 1300 m, where the spectral level is about 10 dB less than that at the corresponding depths in figure 9*a*. The reduced level is almost entirely attributable to the failure of the source to excite the higher-order modes.

A notable feature of figure 9 is the substantial variation of the low-frequency sound field with depth in the upper reaches of the ocean. At 30 Hz, for example, the first peak in figure 9*b* occurs at 300 m, the first trough is at 500 m, and the ratio of the respective spectral levels is approximately 12:1 (10.7 dB). Similar though less pronounced behaviour is exhibited at 20 Hz in figure 9*a*. Variations of such magnitude, which are not confined to the VLF band or the polar oceans (see for example fig. 5 of Farmer & Vagle (1988), showing three time series in a band centred on 4.3 kHz, taken at depths of 1, 10 and 40 m in the open ocean, with levels falling progressively by a total of at least 6 dB), are a factor to be considered in a number of applications, including under-ice acoustic communication. Moreover, the strong depth-dependence of the sound field from a single point source has interesting implications with regard to the ambient noise field in the Arctic Ocean: at the very least, the assumption of spatial homogeneity in the vertical is unlikely to be valid.

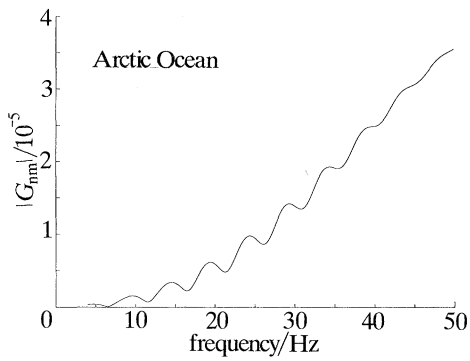

Figure 10. $|G_{nm}|$ (Arctic Ocean) as a function of frequency from (47) ($Q = 1$), with the source and receiver at the same depth (below the surface) of 50 m and separated in range by 10 km.

5.1.2. *Power spectral density*

The spectrum of the field in the Arctic profile, calculated from (47) with the positions of the source and receiver fixed, is shown in figure 10. The ripples in the spectrum are due to the lobular structure in the modes and intermodal interference. As the source is impulsive (i.e. a delta function in time), showing a white spectrum, the very rapid rise in spectral level with increasing frequency represents a genuine transfer characteristic of the inverse-square channel. The increase in level occurs because the number, ΔM, of significant modes in the field approximately scales with frequency.

5.1.3. *Infrasonic ambient noise*

Few if any VLF acoustic transmission experiments in Arctic waters have been reported in the literature, but measurements of the infrasonic ambient noise spectrum in the marginal ice zone (MIZ) off the east Greenland coast have been made by Buckingham (1990*b*) in a continuing series of airborne ocean acoustics experiments in the Nordic Seas. Carefully designed VLF sonobuoys are deployed from a fixed-wing research aircraft into leads of open water between ice floes. Each sonobuoy has a single omnidirectional hydrophone suspended from a surface flotation unit, and the signals are relayed back to the aircraft over a telemetry link. (Occasionally, sonobuoys with horizontal and vertical directivity are also deployed, though the results are not discussed here.) To avoid the severe problems of non-acoustic interference which can be prevalent at infrasonic frequencies (Strasberg 1979) several precautions are taken with the VLF buoys, including the use of flow-shielding on the hydrophones. In the final design, the acoustic signal from these buoys is free of hydrodynamic flow and cable strumming effects down to a frequency of 5 Hz.

The ice cover in the MIZ shows regional, seasonal and interannual variations (Wadhams 1986). Figure 11 shows a high concentration of floes, whose angular shapes indicate recent fracturing due to the action of a heavy sea (predominantly swell). Although not necessarily typical of the MIZ, the high packing density illustrated in the photograph supports the intuitively appealing hypothesis that floe–floe interactions (bumping and rubbing) make a significant contribution to the low-frequency ambient noise in the vicinity of the ice edge. Another possible source of sound is the fracturing process itself.

Figure 11. Recently fractured ice floes and meltwater pools in the MIZ off the east coast of Greenland. The large central floe is about 30 m across. (Aerial photograph by the author.)

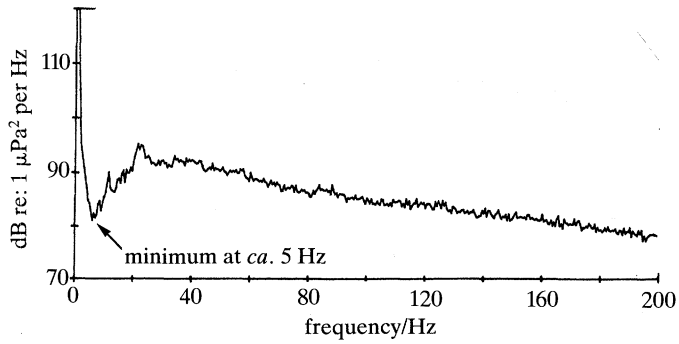

Figure 12. VLF ambient noise spectrum from the MIZ east of Greenland. (76° 37.6′ N, 07° 32.2′ W; hydrophone depth ≈ 160 m; 60 % ice cover; light wind, speed ≈ 3.5 m s^{-1}; sea state, 1–2; swell, nil; visibility greater than 10 km; 4 September 1988.)

Whatever the source mechanism, figure 12 shows an MIZ ambient noise spectrum for low sea-state conditions and moderate ice cover. The averaging was performed over 200 s with a spectral resolution of 0.5 Hz. The pronounced minimum close to 5 Hz is a ubiquitous feature of MIZ infrasonic noise spectra. (A similar minimum, centred at 2–3 Hz, has been observed by Makris & Dyer (1986) in ambient noise spectra recorded under pack ice in the central Arctic.) Between 5 and 20 Hz the steep positive gradient is consistent with the inverse-square spectrum in figure 10, and accordingly is interpreted as an effect of the propagation conditions in the upward refracting Arctic channel (bearing in mind that most of the noise is generated by distant sources). Above 20 Hz the spectrum ceases to rise, probably due to a combination of mechanisms, including absorption in the ocean, acoustic scattering from the surface, and the nature of the source spectrum. Below 5 Hz the very steep negative gradient resembles the spectral shape of ambient noise generated by nonlinear wave–wave interactions (Kibblewhite 1988) but, in view of the partial ice cover and low sea state, is more likely to be an artefact of the measurement system, since it is known that flow noise may be present in this frequency range.

5.2. *Ocean-acoustic tomography: Greenland Sea experiment*

Ocean-acoustic tomography is a technique for mapping the internal structure of the ocean from measurements of the travel times of rays or modes between the elements of a transducer array (Munk & Wunsch 1979). Such an array, of six elements, 200 km aperture, and an operating frequency of 250 Hz, was deployed in September 1988 for about a year at a depth of 95 m in the Greenland Sea, roughly midway between Jan Mayen and Svalbard, under partial ice cover (Guoliang & Wadhams 1989). In this location the water depth is 3660 m.

Based on the profile in figure 5, the structure of the modal field generated by the tomographic sources is readily deduced: the first mode is absent, since its extinction depth is 55.7 m, some 40 m above the array; the extinction depth of the second mode is 99.44 m, so this and higher-order modes are present; and the number of significant modes, ΔM, is approximately 175. Of these modes, numbers 136 (whose extinction depth is 3693 m) and above suffer bottom interactions, as a result of which they are likely to be severely attenuated.

5.2.1. *Group velocity of the modes*

Since the medium is dispersive, the modes show a spread of arrival times. The time for the mth mode to traverse the array is determined by its group velocity, U_m, which from the inverse-square theory is

$$U_m \equiv \frac{\mathrm{d}p_m}{\mathrm{d}\omega} \approx \frac{p_m c_\infty}{k_\infty}\left\{1+\left(\frac{\sigma_m z_1}{\nu z_s}\right)^2\left[1+(m-\tfrac{1}{4})\frac{\pi}{\nu}\right]\right\}^{-1}. \tag{57}$$

Notice that this expression depends on the profile parameters and frequency, but not the depth of the array. Thus, with all else equal, the travel time of a given mode across the array is independent of the position of the array in the water column. Equation (57) is plotted in figure 13 as a function of frequency for a selection of the first 140 modes. Clearly, the high-order modes travel fastest, thus constituting the earliest arrivals. At 250 Hz, modes 2–10 have closely similar group velocities and hence arrive almost simultaneously towards the end of the transmission.

To facilitate interpretation of the tomographic signals, it is desirable that the

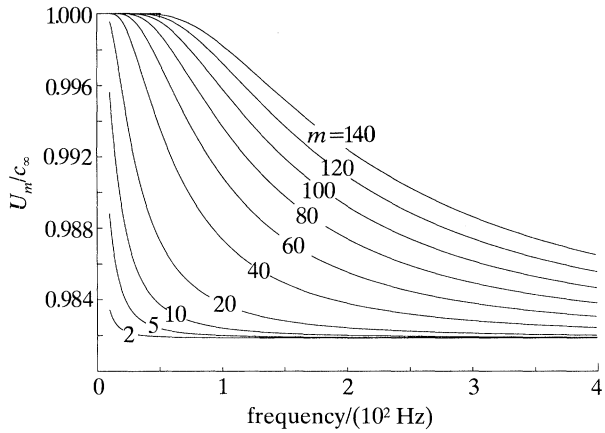

Figure 13. Group velocities of modes in the Arctic profile of figure 5.

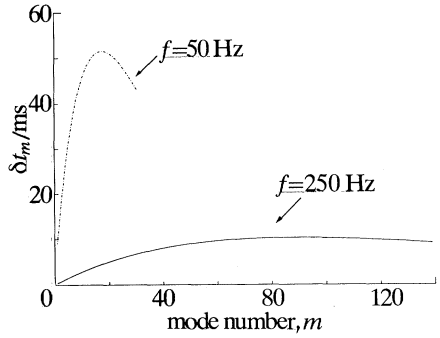

Figure 14. Interval between the arrivals of consecutive modes at a receiver in the Greenland Sea tomographic array.

modal arrivals should be well separated in time. Since the travel time of the mth mode is

$$t_m = L/U_m, \tag{58a}$$

where $L = 200$ km is the aperture of the array, the time interval between consecutive arrivals, say $m+1$ and m, is

$$\delta t_m = t_{m+1} - t_m. \tag{58b}$$

Figure 14 shows δt_m as a function of m. At the operating frequency of 250 Hz, the mean interval between arrivals is $\langle \delta t_m \rangle = 8.3$ ms, although the interarrival times are less than half this value for modes $m < 10$. The duration of the received signals, that is to say the time between the first and last arrivals, is $T = 1.13$ s.

There may be some advantage to be gained by working at a lower frequency. At 50 Hz, for instance, the group velocity curves in figure 13 are well separated for all mode numbers, implying a wider spread of arrival times. In this case, the number of significant modes is $\Delta M \approx 35$, none of which is in extinction. (The extinction depth of the first mode is 169 m.) Modes 28 and above interact with the bottom, and hence are negligible. As shown in figure 14, the interarrival times at 50 Hz are substantially

higher than those for the 250 Hz signal, with a mean time between consecutive arrivals of $\langle \delta t_m \rangle = 41.0$ ms, corresponding to an expansion factor of 5. The duration of the received signal is $T = 1.15$ s.

In addition to the improved arrival structure, losses due to surface scattering and absorption are reduced at lower frequencies, which translates into a higher intensity (or signal-to-noise ratio) at the receiver. This could be beneficial, since timing precision is sacrificed at low signal-to-noise ratios. On the other hand, temporal resolution is inherently poorer at lower frequencies. A further penalty is the implied practical difficulties, notably the size, weight and complexity of the sources.

6. Ambient sound in a bubbly surface duct

Over the past five years or so there has been an accelerating interest in extracting information about the ocean and its boundaries from the ambient noise field that is naturally present below the sea surface. For example, the speed of sound in the bottom sediment has recently been determined by Buckingham & Jones (1987) from measurements of the vertical directionality of the ambient noise field in continental shelf waters at six sites around the coast of the U.K.; the size distribution of bubbles near the surface, in Queen Charlotte Sound, British Columbia, has been estimated by Farmer & Lemon (1984) from measurements of ambient sound at several discrete frequencies between 4.3 and 25 kHz; and surface-wave distributions have been inferred by Farmer & Vagle (1988) from observations of the acoustic signatures of wave-breaking events in the fetch limited environment of Georgia Strait, British Columbia.

With regard to surface processes, ambient sound has the potential, as a remote sensing tool, for providing information on gas fluxes across the air–sea interface, rainfall rates over the ocean, and surface weather conditions in general, including wind speed and direction. To interpret the acoustic observations, however, it is necessary to understand the propagation conditions in the immediate vicinity of the surface. The mechanism which is largely responsible for the acoustic properties of the ocean just below the surface is wave-breaking.

Wave-breaking events entrain air in the ocean, thus creating a bubble layer immediately below the sea surface (Thorpe 1984*a*). The concentration of bubbles decreases rapidly with depth (Thorpe 1984*b*), following an exponential or faster decay law, with an e-folding depth of order 1 m, so most of the bubbles lie within 2–3 m of the surface (Medwin & Breitz 1989). Since a small volume fraction of air (less than 0.01 %) in sea water is sufficient to reduce the sound speed in the medium by several tens of metres per second (Wood 1964), it may be expected that the sound speed is less in this near-surface layer, due to the presence of entrained air, than at greater depths. Indeed, measurements by Farmer & Vagle (1989), hereafter referred to as FV, have confirmed that the sound speed in the near-surface bubble layer increases monotonically with depth, showing a shape that conforms closely with that of the inverse-square profile.

Two examples of bubble layer profiles, as observed by FV near La Perouse Bank, west of Vancouver Island, and in the FASINEX experiment in the North Atlantic, approximately 200 miles southwest of Bermuda, are depicted by the crosses in figure 15. The inverse-square expression in (1) has been fitted to these data points, to yield the solid lines in the figure. The parameters of the profiles are as follows: $z_1 = 0.12$ m, $z_s = 1.8$ m and $c_\infty = 1500$ m s^{-1} (La Perouse); $z_1 = 0.297$ m, $z_s = 1.8$ m and $c_\infty =$

PHILOSOPHICAL TRANSACTIONS OF THE ROYAL SOCIETY A MATHEMATICAL, PHYSICAL & ENGINEERING SCIENCES

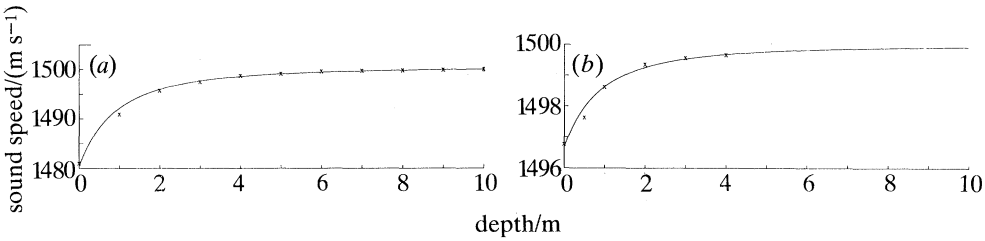

Figure 15. Sound speed profiles for (*a*) La Perouse and (*b*) FASINEX. The crosses are data points taken from FV and the solid lines represent the inverse-square profile (see text for values of the parameters). Notice the different sound speed scales. The effects of dispersion in the bubble layer are negligible at frequencies below 20 kHz.

1500.5 m s^{-1} (FASINEX). Note that the principal difference between these two sets of parameters is in z_1, the effective depth of the channel, the value for FASINEX being larger than that for La Perouse by a factor of about 2.5. A brief account of the range and depth dependence of the modal field in La Perouse profile, as predicted by the inverse-square theory, can be found elsewhere (Buckingham 1991); in the present discussion we shall concentrate on the spectrum, for comparison with the observations of sound produced by individual wave-breaking events reported by FV.

Figure 16 shows two sets of measured spectra, for FASINEX and La Perouse (by courtesy of Farmer & Vagle). These spectra originally appeared as figure 10 of FV. Three wave-breaking signatures, each of duration five seconds or so, are shown for each location. Qualitatively, the spectra from the two sites are quite distinct: those from La Perouse show well-defined spectral *peaks* separated by about 3 kHz, whereas the data from FASINEX are smoother, with the energy distributed in spectral *bands*, which are separated by 'forbidden gaps' roughly 4 kHz apart. For several reasons, including the observation of small shifts in the positions of the peaks and bands from one wave-breaking event to the next, these spectral features are believed to be genuine acoustic effects and not artefacts introduced by the instrumentation (D. M. Farmer, personal communication, 1990).

The spectral structure in both data-sets was interpreted by FV as being due to the wave-guiding effect of the bubble layer. On the basis of an exponential representation of the sound speed profiles for the two sites they derived mode functions, calculated drop-out frequencies (or in their terminology, 'cut-off' frequencies), and attributed the observed spectral features to the drop-out mechanism. However, although there is a rough correspondence between their calculated drop-out frequencies and the positions of the observed peaks in La Perouse, there are subtle differences; and the banding in FASINEX is not explained at all by the drop-out hypothesis. A full analytical description of the spectrum is also absent from the theoretical treatment of FV.

Nevertheless, the wave-guiding effect of the bubble layer does appear to be the physical mechanism responsible for the peaks and bands observed in the wave-breaking spectra, and it is fair to regard the interpretation of FV as a 'first-order' description of the processes involved. A fuller treatment is developed below, based on inverse-square transmission, which as we shall show, not only accounts for the qualitative dissimilarity of the La Perouse and FASINEX spectra, but also provides a complete spectral description of the wave-breaking signatures. The theoretical

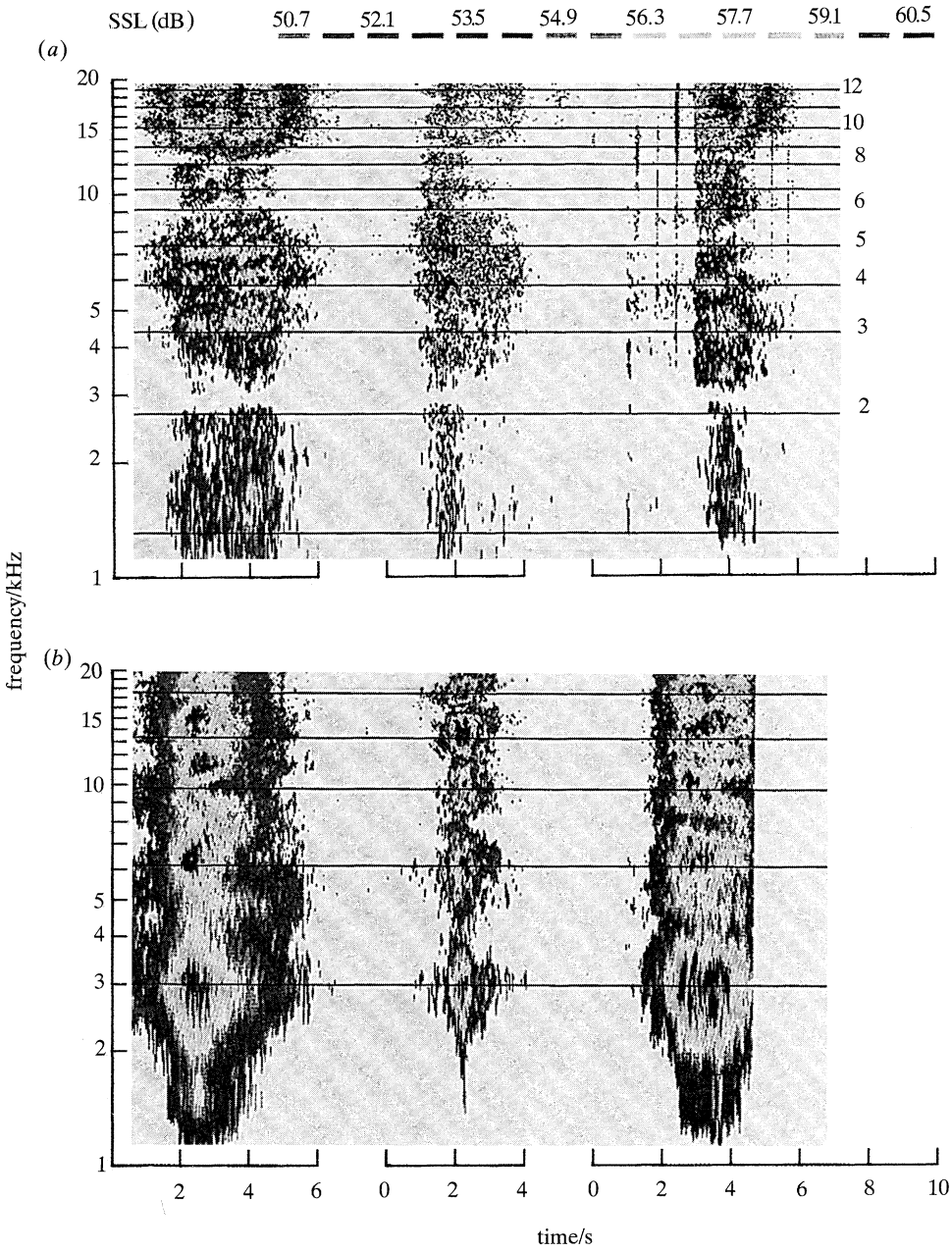

Figure 16. Measured spectra of six wave-breaking events, three in (*a*) FASINEX and three in (*b*) La Perouse. (By courtesy of Farmer & Vagle.) The mean slope has been removed from these spectra to emphasize the rather small spectral modulation. The horizontal lines indicate the mode drop-out frequencies as calculated by Farmer & Vagle from their exponential profile. Almost identical drop-out frequencies emerge from the inverse-square theory (cf. figure 17).

spectrum shows detailed agreement with both data sets. It emerges from the theory that the differences in form between the La Perouse and FASINEX spectra are due solely to the differences between the respective sound speed profiles.

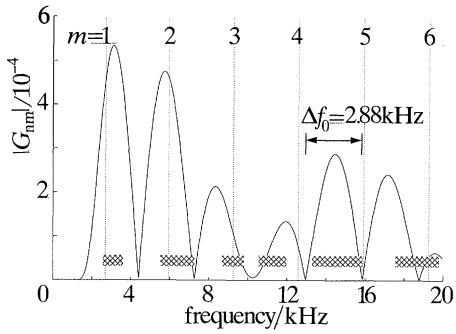

Figure 17. Inverse-square spectrum for the La Perouse profile (solid line), with source depth of 1.5 m, receiver depth of 14 m, both measured from the surface, and horizontal range between source and receiver of 10 m. The vertical dotted lines indicate the drop-out frequencies of modes 1–6, and the horizontal, cross-hatched stripes depict experimentally observed spectral maxima, read from figure 16*b*.

Figures 17 and 19 show the spectra for La Perouse and FASINEX, calculated from the inverse-square modal theory. The receiver depths are 14 m and 24 m, respectively, in accord with the experimental arrangements of FV, the source depth has been chosen as 1.5 m, and in both cases the horizontal range between the source and receiver has been set at 10 m. Each vertical dotted line in figure 17 depicts the drop-out frequency of the indicated mode. Since drop-out is not an abrupt process, due to the evanescent tail on each mode, a given mode will continue to contribute to the field at frequencies slightly above the indicated drop-out frequency.

6.1. *Theory: La Perouse*

Considering La Perouse first, the theoretical spectrum in figure 17 shows well-defined, regularly spaced maxima located approximately 3 kHz apart. These isolated peaks in the inverse-square spectrum can be seen to show no obvious correlation with the computed mode drop-out frequencies (vertical dotted lines), confirming our assertion that the mechanism of mode drop-out is not sufficient in itself to explain the positions of the peaks (and nulls) in the spectrum. In general, the spectral peaks and troughs are a manifestation of *intermode interference*, the detailed structure of the interference pattern being determined by the number, ΔM, of significant modes contributing to the field. Since ΔM increases with rising frequency (see the discussion towards the end of §4.4), the modal interference shows progressively greater complexity in the higher-frequency ranges.

To help clarify the interference mechanism, figure 18 shows the contribution to the La Perouse theoretical spectrum made individually by each of the first six modes (i.e. the magnitude of each term in the mode sum). On comparing figures 17 and 18 it can be seen that the first three (i.e. lowest frequency) peaks in the full spectrum are associated solely with modes 1, 2 and 3, respectively, with interference between modes having little to do with the positions of these maxima. However, the nulls between these peaks are obviously an interference phenomenon. The higher-frequency maxima in the full spectrum are due largely, in this case, to interference between two or more modes. For example, it can be seen from figure 18 that the fifth peak in figure 17, centred just above 14 kHz, results mainly from the coherent addition of modes 4, 5 and 6. For convenience, we shall refer to all such peaks as those

PHILOSOPHICAL TRANSACTIONS OF THE ROYAL SOCIETY A MATHEMATICAL, PHYSICAL & ENGINEERING SCIENCES

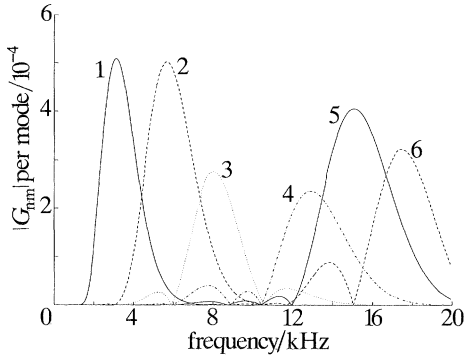

Figure 18. Magnitude of each of the first six modes in the theoretical La Perouse spectrum of figure 17.

in figure 17 as interference maxima, regardless of whether they are associated with only one mode (since this is just a special case of the more general situation) or are the result of constructive interference between several modes.

Clearly, the theoretical peaks in the spectrum of figure 17 are similar to the experimentally observed peaks in figure 16*b*. For a detailed comparison, the bandwidth of each experimental peak has been estimated from figure 16*b* (read at a point 2.4 s into the first event, by which time the wave-breaking is well developed) and superposed on the theoretical spectrum in figure 17 in the form of (six) horizontal cross-hatched stripes. Thus, each stripe represents a spectral region (peak) of high intensity in figure 16*b*. There is clearly a remarkably good correlation between the theory and the observations, with a one-to-one correspondence between the theoretical and experimental spectral maxima. Incidentally, since an impulsive ('white') source was assumed in the derivation of the theoretical spectrum, only the positions and not the relative sizes of the inverse-square peaks are significant with regard to the acoustic signature of wave-breaking events, for in reality the sound is almost certainly generated by a population of bubbles, whose source spectrum is probably far from being white.

6.2. *Theory: FASINEX*

The appearance of well-defined, isolated spectral maxima in the acoustic data from La Perouse may be fortuitous. According to the inverse-square theory (Appendix C), the width of such peaks, Δf_0, depends critically on the size of the parameter z_1: larger values of z_1, characterizing deeper ducts, give rise to a greater number of interfering modes and a higher density of narrower spectral peaks. As it happens, the duct was sufficiently shallow at La Perouse to support, at any given frequency in the experimental range, only two or three significant modes, each of which exhibits well-separated, broad spectral peaks (figures 16*b* and 17). If, in general, surface bubble layers are deeper than that observed at La Perouse, then the resultant, relatively narrow, spectral peaks may be smeared together, due to oceanic fluctuations, in which case observations of individual maxima could be the exception rather than the rule.

In any event, the duct in FASINEX is somewhat deeper than that in La Perouse (recall that the ratio of z_1 (FASINEX) to z_1 (La Perouse) is approximately 2.5:1), and the spectrum (figure 19), according to the inverse-square theory, does indeed show a

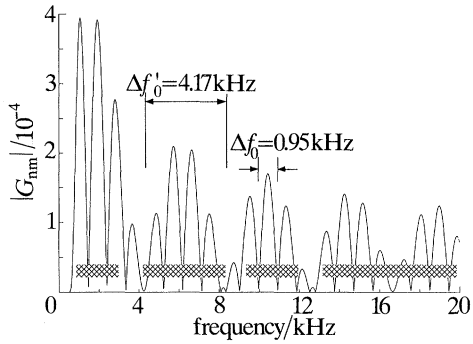

Figure 19. Inverse-square spectrum for the FASINEX profile (solid line), with source depth of 1.5 m, receiver depth of 24 m, both measured from the surface, and horizontal range of 10 m. The horizontal cross-hatched stripes depict the frequency bands where high acoustic energy was observed experimentally, as read from figure 16*a*.

higher density of narrower maxima. (There are about six significant modes at 15 kHz, compared with two for La Perouse.) It is particularly noteworthy that the amplitude of the spectral peaks is modulated by a slowly varying envelope, which clusters the peaks into groups of three or four, to form a spectral band-structure. (A similar modulation is present in the theoretical spectrum for La Perouse in figure 17, though less noticeable because it is so much slower.) As discussed in §6.4, the amplitude modulation is directly related to the source depth. For the prescribed parameters of the FASINEX profile, with a source depth of 1.5 m, the nulls in the envelope ('forbidden gaps') in figure 19 are approximately uniformly spaced and centred on frequencies 4.2, 8.4, 12.6 and 16.8 kHz.

As we have already seen, spectral bands (rather than isolated spectral peaks), separated by 'forbidden gaps', are also a feature of the FASINEX data in figure 16*a*. For comparison with the theory, the width of each band, read from the first event in figure 16*a* at a time of 2.4 s after the onset of wave-breaking, is superposed (the horizontal cross-hatched stripes) on the spectrum in figure 19. Again, the agreement between theory and experiment is compelling. Such accord is all the more remarkable in view of the unsteady, irregular structure of the bubble layer, and the roughness of the sea surface.

To illustrate the complexity of the modal interference mechanism, just four of the modes contributing to the theoretical spectrum in figure 19 are shown in figure 20, that is to say, each curve in the figure represents the magnitude of a single term in the mode sum. Note that each mode shows a multilobe structure, with more peaks appearing in the higher-order modes, to the left of the drop-out frequency. Mode 17, for example, exhibits five maxima between 13 and 20 kHz. The level of the secondary peaks (which were overlooked in FV) may well be comparable with that of the principal maximum.

Each mode occupies a relatively broad frequency band, comparable in width with the centre frequency, as illustrated in figure 20. The mode bandwidth is an ill-defined quantity, but spans the frequency range where the energy in the mode is appreciable. Roughly, this range extends from just above the mode drop-out frequency, at the upper end, down to a frequency below which all the lobes are negligibly small. Thus, the bandwidth of mode 12, for example, is about 11 kHz, with lower and upper limits

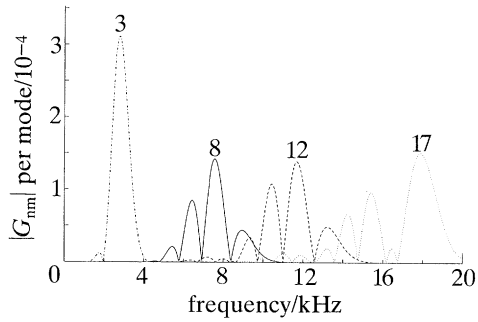

Figure 20. Magnitude of modes 3, 8, 12 and 17 in the theoretical FASINEX spectrum of figure 19.

of 5 and 16 kHz, respectively. At each frequency, of course, a number of modes overlap and combine coherently to form the banded spectrum shown in figure 19.

6.3. *Interpretation of the wave-breaking spectra*

Although the interference mechanism involves an intricate meshing together of modes, the resultant theoretical spectra in figures 17 and 19 show a fairly simple form, consisting of a series of regularly spaced interference peaks, which are slowly modulated by an envelope function. A simple argument, developed in Appendix C, shows that the interference peaks are governed by the receiver eigenfunction in the mode sum, whereas the modulation is controlled by the source eigenfunction. The width of the interference peaks is

$$\Delta f_0 \approx c_\infty / 2 z_1 \ln (z/z_s), \tag{59a}$$

with an analogous expression holding for the broader maxima in the modulation:

$$\Delta f_0' \approx c_\infty / 2 z_1 \ln (z'/z_s). \tag{59b}$$

The spectra from La Perouse in figure 16*b* show little evidence of modulation but the width of the spectral peaks is very close to the theoretical value $\Delta f_0 \approx 2.88$ kHz calculated from (59*a*), as expected from the correspondence between theory and experiment in figure 17. Conversely, the FASINEX spectra in figure 16*a* show a pronounced modulation structure (the spectral bands), with little sign of spectral peaks within the bands. The width of each band, according to (59*b*), is $\Delta f_0' \approx 4.17$ kHz, confirming the agreement between theory and experiment that has already been demonstrated in figure 19. A closer examination of the FASINEX data reveals traces of high intensity spectral peaks within the band from 4 to 8 kHz, and the width of these vestigial peaks is consistent with the value $\Delta f_0 \approx 0.95$ kHz calculated from (59*a*).

We are now in a position to explain the qualitative differences between the La Perouse and FASINEX spectra. The well-defined spectral peaks in La Perouse arise from modal interference; and the apparent absence of amplitude modulation is attributed to the fact that, because the channel is so shallow ($z_1 = 0.12$ m), the modulation is too slow to be discernible ($\Delta f_0' \approx 10.31$ kHz). In FASINEX, on the other hand, the channel is 2.5 times deeper ($z_1 = 0.297$ m) than that in La Perouse, hence the modulation is faster and is perceived as the broad band structure in the measured spectra. The 'forbidden gaps' between the bands correspond to nulls in the modulation envelope. Within the bands in the FASINEX spectra, the barely discernible

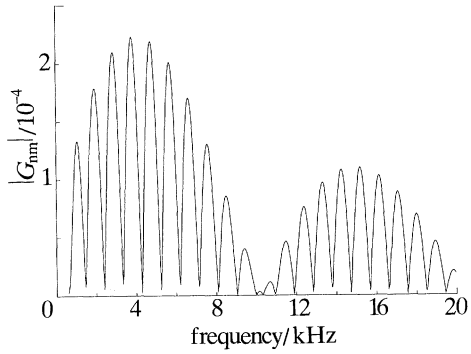

Figure 21. Inverse-square spectrum for FASINEX, as in figure 17, except that the source depth is reduced to 0.5 m. With this shallower setting the modulation does not match the data in figure 16*a*.

fine structure (apparent in the original colour plates in FV) can be identified with the narrow interference peaks, which have probably suffered a certain degree of spectral smearing as a result of oceanic fluctuations.

6.4. *Inverse solution for the source depth*

The presence of z' in (59*b*) implies that a direct measure of the source depth can be obtained from the spectral period, $\Delta f'_0$, of the modulation, provided the parameters of the profile are known. Thus, we have a solution to the inverse problem of determining the source depth, $d' \equiv (z' - z_s)$, once the spectrum is known. To be explicit, from (59*b*),

$$d' \equiv (z' - z_s) = z_s\{\exp(c_\infty/2z_1\,\Delta f'_0) - 1\}. \tag{60}$$

Regarding this expression as an estimator of the source depth, suppose we consider the width of the modulation required to produce a reduction in d' by a factor of three, to 0.5 m: $\Delta f'_0 \approx 10.31$ kHz. The associated inverse-square spectrum is illustrated in figure 21, from which it is clear that the nulls in the envelope no longer match the 'forbidden gap' structure in the FASINEX data. On this basis it appears that the modulation structure is a sensitive, robust indicator of source depth.

The close correspondence between the theoretical and experimental 'forbidden gaps' in figure 19 suggests that the source depth of 1.5 m emerging from the inverse-square theory is representative of the actual depth of the sources in the FASINEX experiment. It is not clear why the sources should be so deep, although it is not inconceivable that a number of acoustically active bubbles were concentrated around a depth of 1.5 m. There is little doubt, from the measured backscatter cross sections for the FASINEX area, shown in fig. 5*a* of FV, that a high concentration of bubbles did exist down to a depth of about 1.5 m beneath the surface, but presumably these bubbles were mostly mature and therefore quiescent. From the available supporting information, it is not possible to establish independently the depth distribution of the acoustically active bubbles in FASINEX. And as the La Perouse data show little evidence of a modulation structure, they do not provide an additional source of information on the depth of the acoustic sources. (One might surmise that as the bubble layer is shallower in La Perouse so too are the sources.)

To speculate as to why bubbles at the bottom of the surface layer should be more effective acoustic radiators than those nearer the surface is likely to prove fruitless

in the absence of more details on both the bubbles' dynamics and the processes which influence acoustic propagation through the bubbly medium (including absorption, re-radiation and scattering by other bubbles in the layer). It should be mentioned that the roughness of the sea surface could, perhaps, be responsible for leading to an exaggerated estimate of the depth of the bubble sources. Although this cannot be entirely discounted, the detailed correspondence between the theoretical and observed spectra indicates that, at least over horizontal ranges which are shorter than the wavelength of the dominant surface waves, the bubble layer behaves as a deterministic waveguide with a planar, pressure-release boundary. If surface roughness were a significant factor, such behaviour would not be expected.

Since the spectra reported by FV were all recorded under similar wind speeds, around 10 to 12 m s^{-1}, it would be of considerable interest to examine data taken under different wind conditions (as suggested by M. S. Longuet-Higgins, personal communication, 1990), to establish the effect of wind speed on the modulation structure. With the expression in (60), it should then be possible to determine the depth of the acoustic sources as a function of wind speed. This may help resolve some of the questions to which we have already alluded, particularly those concerning the significance of multiple scattering. At present, apart from the inference drawn above that the principal FASINEX sources are located at a depth of 1.5 m, no information on the depth distribution of acoustically active bubbles in the ocean is known to the author. (Oscillating bubbles from spilling breakers have been observed within a few millimetres of the surface by Medwin & Beaky (1989) and Medwin & Daniel (1990) under wind-free conditions in a laboratory tank; and in similar circumstances Melville *et al.* (1988) have shown that there is a strong correlation between the microwave return from a breaking wave and its sub-surface acoustic signature.)

6.5. *Alternative mechanisms*

The detailed correlation between the inverse-square theory and experiment lends support to the conclusion that, in general, intermode interference is the mechanism responsible for well-defined spectral peaks in shallow bubble layers, or broader spectral bands in deeper ducts, in the acoustic signatures of wave-breaking events. Of the two alternative mechanisms that have been proposed, one is mode drop-out on its own, or more specifically, the appearance of a peak in the spectrum just below the drop-out frequency of each mode. This mechanism is the basis of the analysis in the pioneering paper by FV. But as we have seen (figure 17), the drop-out frequencies show subtle but distinct deviations from the positions of the peaks in the La Perouse data; and the drop-out process is unrelated to the spectral banding observed in FASINEX. The second proposal, by Longuet-Higgins (1990), attributes the observed spectral phenomena to the source rather than the propagation conditions. He invokes resonances in nonlinear bubble oscillations as the mechanism responsible for the observed spectral peaks, and shows that such resonances can give rise to significant levels of sound in the ocean at well-defined frequencies in the band between 1 and 100 kHz.

The nonlinear shape-oscillation mechanism may account for the appearance of peaks in bubble-noise spectra taken in a laboratory tank, with no wind over the surface, as observed by Medwin & Beaky (1989) and Medwin & Daniel (1990). Such oscillations may also be at least partly responsible for the presence of spectral peaks in McConnell's (1983) measurements of background noise in the Pacific with a hydrophone at a depth of 60 m, well below the surface bubble layer. A similar

PHILOSOPHICAL TRANSACTIONS OF THE ROYAL SOCIETY A MATHEMATICAL, PHYSICAL & ENGINEERING SCIENCES

comment applies to the noise data from the Behm Canal, Alaska, taken by McConnell & Schilt (1989), with a hydrophone at a depth of 120 m. But in open-ocean observations with the hydrophone located in or close to the bubble layer, as in the La Perouse and FASINEX experiments conducted by FV, the factor governing the structure of the noise spectrum would seem to be the upward-refractive propagation conditions.

7. Concluding remarks

Immediately below the surface of the ocean the variation of sound speed with depth often takes a form that can be accurately represented by an inverse-square profile. Examples include the surface channel in the mixed layer and the upward-refracting stratification found in polar waters. In such conditions, acoustic energy, especially at low frequencies, may propagate to long ranges in the form of normal modes.

An exact, complete theory of acoustic propagation in an inverse-square profile, developed above, shows that the total field consists of the normal mode component plus a near-field, branch line integral that gives the field singularity at the source position. Certain unusual aspects of the branch line integral have been mentioned in this paper, although the main emphasis has been placed on the normal mode sum because, in many experimental situations, it is the far field that is of paramount importance. The properties of the modes have been fully established from relatively simple expressions derived from first- and second-order asymptotics. These expressions provide extensive information on the physical characteristics of the modes, which, as it turns out, are quite different from the properties of modes in a waveguide with plane, parallel boundaries. In particular, there is no mode cut-off and there are no evanescent modes in the inverse-square profile.

A mode in the inverse-square profile shows an oscillatory region immediately beneath the surface down to the extinction depth, below which it decays exponentially to zero. Thus, although there are no evanescent modes in the duct, there is an evanescent region in the depth profile of each mode. The extinction depth, marking the onset of the evanescent region, increases exponentially with the mode number, that is to say, the higher-order modes penetrate deeper into the water column. A reciprocal relationship exists between the extinction depth and the strength of a mode, indicating that the deeper modes contribute proportionately less to the mode sum.

The extinction depth is also a function of frequency, decreasing (i.e. approaching the surface) rapidly as the frequency rises. This behaviour is responsible for the phenomenon of mode drop-out, whereby the extinction depth of the first mode, followed by that of the second, third, fourth and so on, passes through a receiver at fixed depth as the frequency increases. After drop-out, a mode soon ceases to contribute to the field observed at the receiver.

Well above the extinction depth, the zeros show the same depth distribution in all the modes. A consequence of this nodal distribution, which is logarithmic in depth, is that multimode suppression can be achieved in the inverse-square profile. By placing a receiver at a depth corresponding to the depth of the node, most of the modes are either nullified or in extinction, leaving a package of three or four modes as the sole constituents of the field. One effect of multimode suppression is that the field along the channel is considerably smoother than it would be in the presence of interference from all the modes.

PHILOSOPHICAL TRANSACTIONS OF THE ROYAL SOCIETY A MATHEMATICAL, PHYSICAL & ENGINEERING SCIENCES

The inverse-square theory provides a reliable, robust means of investigating acoustic propagation in a variety of conditions encountered in the ocean. This is illustrated through an examination of inverse-square transmission in two very different types of ocean-acoustic environment, the Arctic Ocean and the surface bubble layer in the open ocean. Long-range acoustic propagation is supported in the upward refractive conditions of the Arctic Ocean, as discussed in connection, firstly, with recent observations of infrasonic ambient noise in the MIZ off the east coast of Greenland and, secondly, with an under-ice ocean-acoustic tomography experiment in the Greenland Sea. On a depth scale that is smaller by several orders of magnitude, our second environment, the ocean-surface bubble layer, acts as a surface duct for frequencies in the audio-frequency range above about 2 kHz. In both the Arctic Ocean and the surface bubble layer, the upward refracting nature of the medium has a profound effect on the properties of the sound field at the receiver.

In the case of the bubble layer, the inverse-square theory reproduces in detail the spectral features observed by Farmer & Vagle (1989) in the acoustic signatures of wave-breaking events. Specifically, these features take the form of spectral peaks in the La Perouse data and broader spectral bands in the FASINEX events. Our conclusion is three-fold: firstly, the spectral features in both data-sets are manifestations of wave-guide propagation, which arises from the upward-refracting condition existing in the bubbly surface layer; secondly, the qualitative differences between the two types of spectra may be attributed to differing channel depths, FASINEX being 2.5 times deeper than La Perouse, hence supporting proportionately more modes; and thirdly, near-surface measurements of bubble-layer spectra, in combination with the inverse-square theory, have the potential for determining the source depth provided the profile parameters are known, or conversely, for determining the profile given the receiver and source depths.

It is a pleasure to acknowledge many interesting discussions on near-surface bubble layers with Dr David Farmer and Professor Michael Longuet-Higgins. Julian Fletcher of the Royal Aerospace Establishment, Farnborough, U.K., has efficiently organized the Arctic acoustic airborne-measurement programme from its inception. The professional expertize and good humour of the aircrews of the Experimental Flying Department, RAE, is especially appreciated. Partial support for the research was received from the U.S. Office of Naval Research under contracts N00014-89-K-0038 and N00014-80-C-0220.

Appendix A. Normal modes and the branch line integral

Equation (28) expresses the field as the sum of two integrals,

$$G = \tfrac{1}{16}\mathrm{j}\,\mathrm{Q}\sqrt{(zz')}\,\{I_1 + I_2\}, \tag{A 1}$$

where

$$I_1 = \int_0^\infty pS_\mu(\eta)\,H_0^{(1)}(pr)\,\mathrm{d}p, \tag{A 2}$$

$$I_2 = \int_0^\infty pS_\mu(\eta)\,H_0^{(2)}(pr)\,\mathrm{d}p, \tag{A 3}$$

and

$$S_\mu(\eta) = [H_\mu^{(1)}(\eta z')/H_\mu^{(1)}(\eta z_\mathrm{s})][H_\mu^{(2)}(\eta z)\,H_\mu^{(1)}(\eta z_\mathrm{s}) - H_\mu^{(1)}(\eta z)\,H_\mu^{(2)}(\eta z_\mathrm{s})], \quad \text{for} \quad z' > z. \tag{A 4}$$

The radical

$$\eta = \sqrt{(k_\infty^2 - p^2)} \tag{A 5}$$

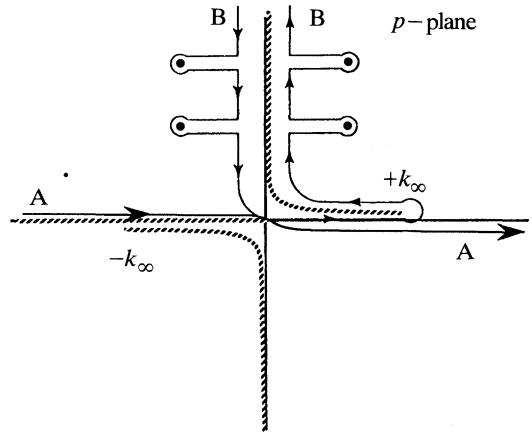

Figure 22. Branch cuts (hatched lines) for $S_\mu(\eta)$, beginning at $\pm k_\infty$ (which is assumed to have a infinitesimal imaginary component); and for the Hankel functions, along the negative real axis. Contour (A–A) of integration for the integral I is deformed (B–B) to follow the upper branch cut enclosing the poles of $S_\mu(\eta)$.

in these expressions has branch points at $p = \pm k_\infty$, implying that two branch cuts must be made in the complex p-plane to avoid ambiguity in $S_\mu(\eta)$. The cut lines are chosen in such a way that $\mathrm{Im}\,(\eta) > 0$ over the entire top Riemann sheet, to ensure convergence of $S_\mu(\eta)$ everywhere on the sheet. Figure 22 shows the appropriate choice for these branch lines, and also the branch cut along the negative real axis associated with the Hankel functions in (A 2) and (A 3).

Turning to the integral I_2, the substitution

$$q = p\,\mathrm{e}^{\mathrm{j}\pi}, \tag{A 6}$$

leads to the formulation

$$I_2 = \mathrm{e}^{-2\mathrm{j}\pi} \int_0^{\infty \exp \mathrm{j}\pi} q S_\mu(\eta_q)\, H_0^{(2)}(qr\,\mathrm{e}^{-\mathrm{j}\pi})\,\mathrm{d}q, \tag{A 7}$$

where

$$\eta_q = \sqrt{(k_\infty^2 - q^2\,\mathrm{e}^{-2\mathrm{j}\pi})} = \sqrt{(k_\infty^2 - q^2)}. \tag{A 8}$$

As

$$H_0^{(2)}(qr\,\mathrm{e}^{-\mathrm{j}\pi}) = -H_0^{(1)}(qr), \tag{A 9}$$

it follows that

$$I_2 = -\int_0^{\infty \exp \mathrm{j}\pi} q S_\mu(\eta_q)\, H_0^{(1)}(qr)\,\mathrm{d}q$$

$$\equiv -\int_0^{\infty \exp \mathrm{j}\pi} p S_\mu(\eta)\, H_0^{(1)}(pr)\,\mathrm{d}p, \tag{A 10}$$

and hence the integral I is

$$I = \int_{\infty \exp \mathrm{j}\pi}^{\infty} p S_\mu(\eta)\, H_0^{(1)}(pr)\,\mathrm{d}p, \tag{A 11}$$

where the path of integration is designated A–A in figure 22.

Since $\mathrm{Im}\,(\eta) > 0$, it follows that $S_\mu(\eta) \to 0$ when $|p| \to \infty$ everywhere on the top sheet. Therefore, the contour A–A in figure 22 may be deformed to follow the upper branch cut, thus enclosing all the poles of $S_\mu(\eta)$ in the upper half-plane (contour B–B

in figure 22). The contribution to the integral from the infinitesimal circle surrounding the branch point at $p = k_\infty$ is zero and the net contribution from the outward and return paths to the poles is also zero. From Cauchy's theorem, the integral I is equal to the integral along the section of path B–B with arrows plus the sum of the residues, R_m, from the poles:

$$I = \int p S_\mu(\eta)\, H_0^{(1)}(pr)\, \mathrm{d}p + 2\pi \mathrm{j} \sum_{m=1}^{\infty} R_m. \tag{A 12}$$

By changing the integration variable from p to η, and recognizing that $\eta = +\infty$ at the beginning of the path and $\eta = -\infty$ at the end of the path, this expression becomes

$$I = \int_{-\infty}^{\infty} \eta S_\mu(\eta)\, H_0^{(1)}(\sqrt{(k_\infty^2 - \eta^2)}\, r)\, \mathrm{d}\eta + 2\pi \mathrm{j} \sum_{m=1}^{\infty} R_m. \tag{A 13}$$

The residues can be written down immediately from (A 4):

$$R_m = \frac{\eta_m H_\mu^{(1)}(\eta_m z)\, H_\mu^{(1)}(\eta_m z')\, H_\mu^{(2)}(\eta_m z_\mathrm{s})}{\partial H_\mu^{(1)}(\eta z_\mathrm{s})/\partial \eta\,|_{\eta=\eta_m}} H_0^{(1)}(\sqrt{(k_\infty^2 - \eta_m^2)}\, r), \tag{A 14}$$

where η_m is the mth root of the equation

$$H_\mu^{(1)}(\eta z_\mathrm{s}) = 0. \tag{A 15}$$

Therefore, the field G in (A 1) consists of a branch line integral, G_bl, plus a sum of normal modes, G_nm:

$$G = G_\mathrm{bl} + G_\mathrm{nm}, \tag{A 16}$$

where

$$G_\mathrm{bl} = \frac{\mathrm{j}Q\sqrt{(zz')}}{16} \int_{-\infty}^{\infty} \eta S_\mu(\eta)\, H_0^{(1)}(\sqrt{(k_\infty^2 - \eta^2)}\, r)\, \mathrm{d}\eta \tag{A 17}$$

and

$$G_\mathrm{nm} = -\frac{Q\pi\sqrt{(zz')}}{8} \sum_{m=1}^{\infty} \frac{\eta_m H_\mu^{(1)}(\eta_m z)\, H_\mu^{(1)}(\eta_m z')\, H_\mu^{(2)}(\eta_m z_\mathrm{s})}{\partial H_\mu^{(1)}(\eta z_\mathrm{s})/\partial \eta\,|_{\eta=\eta_m}} H_0^{(1)}(\sqrt{(k_\infty^2 - \eta_m^2)}\, r). \tag{A 18}$$

Equations (A 17) and (A 18) are exact expressions for the field whose properties are discussed in the text.

Appendix B. Asymptotic analyses of $H_{-\mathrm{j}\nu}^{(1)}(\mathrm{j}\sigma)$

The normal modes in the inverse-square profile are specified by the Hankel function $H_{-\mathrm{j}\nu}^{(1)}(\mathrm{j}\sigma)$, which has the following integral representation (Watson 1958):

$$H_{-\mathrm{j}\nu}^{(1)}(\mathrm{j}\sigma) = \frac{\mathrm{e}^{-\nu\pi/2}}{\mathrm{j}\pi} \int_{-\infty}^{\infty} \exp\{\mathrm{j}\nu u - \sigma\cosh(u)\}\, \mathrm{d}u. \tag{B 1}$$

On taking this integral, F, around the rectangular contour in figure 23, it follows from Cauchy's theorem, since there are no poles within the contour and the contributions from the vertical segments are identically zero, that

$$F = \int_{\infty+\mathrm{j}\pi/2}^{-\infty+\mathrm{j}\pi/2} \exp\{\mathrm{j}\nu u - \sigma\cosh(u)\}\, \mathrm{d}u. \tag{B 2}$$

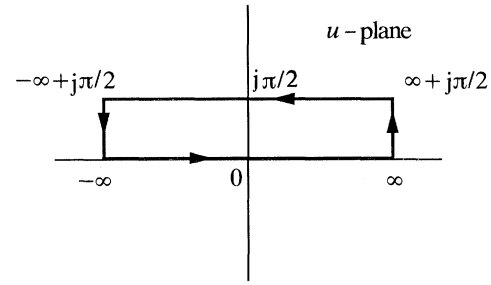

Figure 23. Rectangular contour in the u-plane for integral F.

By making a change of variable to $u-\frac{1}{2}\mathrm{j}\pi$, we obtain

$$H^{(1)}_{-\mathrm{j}\nu}(\mathrm{j}\sigma) = -\frac{\mathrm{e}^{-\nu\pi}}{\mathrm{j}\pi}\int_{-\infty}^{\infty}\exp \mathrm{j}\{\nu u-\sigma\sinh(u)\}\,\mathrm{d}u. \tag{B 3}$$

For $\nu > \sigma$ this integral may be evaluated by the method of stationary phase.

The phase function and its first three derivatives with respect to u are

$$y = u-(\sigma/\nu)\sinh(u), \tag{B 4a}$$

$$y' = 1-(\sigma/\nu)\cosh(u), \tag{B 4b}$$

$$y'' = -(\sigma/\nu)\sinh(u), \tag{B 4c}$$

and

$$y''' = -(\sigma/\nu)\cosh(u). \tag{B 4d}$$

The two turning points, u_1 and u_2, obtained by equating the first derivative to zero, are given by

$$\cosh(u_{1,2}) = \nu/\sigma, \tag{B 5a}$$

or explicitly,

$$u_1 = -u_2 = \ln[(\nu+\sqrt{(\nu^2-\sigma^2)})/\sigma]. \tag{B 5b}$$

From standard first-order stationary phase theory, since there are no end point contributions, it follows that

$$H^{(1)}_{-\mathrm{j}\nu}(\mathrm{j}\sigma) \approx -\frac{2\mathrm{e}^{-\nu\pi}}{\mathrm{j}\pi}\frac{\sqrt{(2\pi)}}{(\nu^2-\sigma^2)^{\frac{1}{4}}}\cos\left\{\nu\ln\left[\frac{\nu+\sqrt{(\nu^2-\sigma^2)}}{\sigma}\right]-\sqrt{(\nu^2-\sigma^2)}-\tfrac{1}{4}\pi\right\}, \tag{B 6}$$

which is an oscillatory expression that is valid provided σ is somewhat less than ν.

When σ takes values close to ν, the turning points both approach zero and the second derivatives $y''(u_{1,2})$ in (B 4c) also go to zero. As these second derivatives appear in the denominator of (B 6), first-order stationary phase fails under these conditions and it is necessary to turn to second-order asymptotics.

Following Pekeris (1948), the phase function, $y(u)$, is expanded in a Taylor series about $u = 0$. At $u = 0$ the phase function itself and its second derivative, $y''(u)$ are identically zero and hence, to third order in u,

$$y(u) \approx (1-\sigma/\nu)\,u-(\sigma/6\nu)\,u^3. \tag{B 7}$$

On substituting this expression into the integral in (B 3), and changing the range of integration from 0 to ∞, the expression for the Hankel function becomes

$$\begin{aligned} H^{(1)}_{-\mathrm{j}\nu}(\mathrm{j}\sigma) &\approx -\frac{2\mathrm{e}^{-\nu\pi}}{\mathrm{j}\pi}\int_0^{\infty}\cos\{\tfrac{1}{6}\sigma u^3-(\nu-\sigma)\,u\}\,\mathrm{d}u \\ &= 2\mathrm{j}\mathrm{e}^{-\nu\pi}(2/\sigma)^{\frac{1}{3}}\,\mathrm{Ai}[(2/\sigma)^{\frac{1}{3}}(\sigma-\nu)], \end{aligned} \tag{B 8}$$

where Ai[ ] is an Airy function of the first kind. This second-order expression in conjunction with the first-order result in (B 6) accurately represents the Hankel function of the first kind of imaginary order and imaginary argument over the full range of σ.

Appendix C. Spectral periodicity in the mode sum

To understand the quasi-periodicity of the observed spectra from wave-breaking events, it is necessary to examine the frequency dependence of the mode functions in the inverse-square theory. Since we are interested here primarily in the oscillatory part of the modes, the asymptotic solution in (36*a*) provides the basis for discussion.

On neglecting the term in σ_m in all the radicals, the receiver mode function reduces to

$$U_\nu(\sigma_m \zeta) \approx -2\sqrt{(2/\pi\nu)}\cos\{\nu[\ln(2\nu/\sigma_m \zeta)-1]-\tfrac{1}{4}\pi\}. \tag{C 1}$$

From (44),
$$2\nu/\sigma_m \approx \exp\{m\pi/\nu+1-\pi/4\nu\}, \tag{C 2}$$

and hence the mode function is approximated by

$$\begin{aligned} U_\nu(\sigma_m \zeta) &\approx -2\sqrt{(2/\pi\nu)}\sin\{m\pi-\nu\ln(\zeta)\} \\ &= 2\sqrt{(2/\pi\nu)}\,(-1)^m \sin\{\nu\ln(\zeta)\}. \end{aligned} \tag{C 3}$$

Naturally a similar expression, with ζ' in place of ζ, holds for the source modes. As (C 3) is independent of mode number (apart from the sign), it follows that, through ν, which essentially scales with frequency, all the modes show the same dependence on the acoustic frequency (at least to the level of approximation given here). In other words, in the frequency domain, each mode is oscillatory with spectral period and phase that are independent of mode number. (The amplitude, of course, takes significant non-zero values only below the drop-out frequency, which is a function of mode number.)

When (C 3) is substituted into (47), the mode sum can be approximated as

$$G_{\mathrm{nm}} \approx -\frac{Q\sqrt{(zz')}}{2\nu^2 z_{\mathrm{s}}^2}\sin(\nu\ln\zeta)\sin(\nu\ln\zeta')\sum_{m=1}^{\infty}\sigma_m^2 H_0^{(1)}\left(\sqrt{(k_\infty^2 z_{\mathrm{s}}^2+\sigma_m^2)}\,\frac{r}{z_{\mathrm{s}}}\right). \tag{C 4}$$

The mode functions now appear as a product outside the summation, representing a modulated, periodic waveform: since $\zeta' \ll \zeta$ in La Perouse and FASINEX, we see that the receiver-mode function (involving ζ) gives rise to a series of regularly spaced spectral maxima (the interference peaks, prominent in the La Perouse spectra), which are modulated by the slower source-mode function (involving ζ'). (The modulation is the dominant effect in the FASINEX spectra.) The separation, Δf_0, of the zeros in the receiver mode function (i.e. the bandwidth of a spectral peak) is obtained by setting the argument of the sine function in (C 3) equal to π:

$$\Delta f_0 \approx c_\infty/[2z_1\ln(z/z_{\mathrm{s}})]. \tag{C 5}$$

Similarly, the separation, $\Delta f_0'$, of the zeros in the source mode function (i.e. the spectral period of the modulation) is

$$\Delta f_0' \approx c_\infty/[2z_1\ln(z'/z_{\mathrm{s}})]. \tag{C 6}$$

If the parameters of the profile are known, then these two expressions permit the source and receiver depths to be determined from a measurement of the spectrum. Conversely, the profile parameters can be estimated if z and z' are known.

References

Abramowitz, M. & Stegun, I. A. 1965 *Handbook of mathematical functions*. New York: Dover.

Arfken, G. 1966 *Mathematical methods for physicists*, p. 395. New York: Academic Press.

Balogh, C. B. 1967 Asymptotic expansions of the modified Bessel function of the third kind of imaginary order. *SIAM J. appl. Math.* **15**, 1315–1323.

Buckingham, M. J. 1988 Spherically symmetrical acoustic propagation across a fluid/fluid boundary. *J. acoust. Soc. Am.* **83**, 566–570.

Buckingham, M. J. 1990*a* The role of analytical modelling in modern ocean acoustics. *Computational acoustics, seismo-ocean acoustics and modelling*, pp. 89–105. Amsterdam: Elsevier.

Buckingham, M. J. 1990*b* Ambient sound at the ice edge. *Proc. Undersea Defence Technology Conference, Novotel, London*, 7–9 February, pp. 189–194.

Buckingham, M. J. 1991 Ocean acoustic propagation and ambient noise in a surface duct. In *Natural physical sources of underwater sound* (ed. B. R. Kerman). Kluwer.

Buckingham, M. J. & Jones, S. A. S. 1987 A new shallow-ocean technique for determining the critical angle of the seabed from the vertical directionality of the ambient noise in the water column. *J. acoust. Soc. Am.* **81**, 938–946.

Cochran, J. A. 1965 The zeros of Hankel functions as functions of their order. *Numerische Mathematik* **7**, 238–250.

Di Napoli, F. R. 1971 Fast field program for multilayered media. *Naval Underwater Systems Center Tech. Rep.* 4103.

Dorman, J. 1962 Period equations for waves of Rayleigh type on a layered liquid–solid half-space. *Bull. Seismolog. Soc. Am.* **52**, 389–397.

Erdélyi, A. (ed.) 1954 The Bateman Project Staff: *Tables of integral transforms*, vol. 2, p. 9. New York: McGraw-Hill.

Farmer, D. M. & Lemon, D. D. 1984 The influence of bubbles on ambient noise in the ocean at high wind speeds. *J. Phys. Ocean.* **14**, 1762–1778.

Farmer, D. M. & Vagle, S. 1988 On the determination of breaking surface wave distributions using ambient sound. *J. geophys. Res.* **93**, 3591–3600.

Farmer, D. M. & Vagle, S. 1989 Waveguide propagation of ambient sound in the ocean-surface bubble layer. *J. acoust. Soc. Am.* **86**, 1897–1908.

Felsen, L. B. & Marcuvitz, N. 1973 *Radiation and scattering of waves*, pp. 595–606. Englewood Cliffs, New Jersey: Prentice-Hall.

Furry, W. H. 1951 The bilinear modified index profile. In *Propagation of short radio waves* (ed. D. E. Kerr), pp. 140–174. New York: McGraw-Hill.

Guoliang, J. & Wadhams, P. 1989 Travel time changes in a tomography array caused by a sea ice cover. *Prog. Oceanogr.* **22**, 249–275.

Harrison, C. H. 1989 Ocean propagation models. *Appl. Acoust.* **27**, 163–201.

Jeng, S. K. & Liu, C. H. 1987 Wave propagation in media with three-dimensional quadratic refractive index profile. *J. acoust. Soc. Am.* **81**, 1732–1740.

Jones, D. S. 1986 *Acoustic and electromagnetic waves*. Oxford: Clarendon Press.

Keller, J. B., Rubinow, S. I. & Goldstein, M. 1963 Zeros of Hankel functions and poles of scattering amplitudes. *J. math. Phys.* **4**, 829–832.

Kibblewhite, A. C. 1988 Ocean noise spectrum below 10 Hz – mechanisms and measurements. In *Sea surface sound* (ed. B. R. Kerman), pp. 337–359, NATO ASI Series. Kluwer.

Kuperman, W. A. 1988 Propagation effects associated with ambient noise. In *Sea surface sound* (ed. B. R. Kerman), pp. 253–272, NATO ASI Series. Kluwer.

Kutschale, H. W. 1973 Rapid computation by wave theory of propagation loss in the Arctic Ocean. Rep. no. CU-8-73. Columbia University, Palisades, New York.

Labianca, F. M. 1973 Normal modes, virtual modes, and alternative representations in the theory of surface-duct sound propagation. *J. acoust. Soc. Am.* **53**, 1137–1147.

Langer, R. E. 1932 On the asymptotic solutions of differential equations, with an application to the Bessel functions of large complex order. *Trans. Am. math. Soc.* **34**, 447–480.

PHILOSOPHICAL TRANSACTIONS OF THE ROYAL SOCIETY A MATHEMATICAL, PHYSICAL & ENGINEERING SCIENCES

Langer, R. E. 1949 The asymptotic solutions of ordinary linear differential equations of the second order, with special reference to a turning point. *Trans. Am. math. Soc.* **67**, 461–490.

Lebedev, N. N. 1965 *Special functions and their applications* (transl. by R. A. Silverman). Englewood Cliffs, New Jersey: Prentice-Hall.

Li, Y. L., Liu, C. H. & Franke, S. J. 1990 Three-dimensional Green's function for wave propagation in a linearly inhomogeneous medium – the exact analytic solution. *J. acoust. Soc. Am.* **87**, 2285–2291.

Longuet-Higgins, M. S. 1990 Bubble noise spectra. *J. acoust. Soc. Am.* **87**, 652–661.

Magnus, W. & Kotin, L. 1960 The zeros of the Hankel function as a function of its order. *Numerische Mathematik* **2**, 228–244.

Makris, N. C. & Dyer, I. 1986 Environmental correlates of pack ice noise. *J. acoust. Soc. Am.* **75**, 1434–1440.

McConnell, S. O. & Schilt, M. P. 1989 Ambient noise measurements from 100 Hz to 80 kHz. *J. acoust. Soc. Am.* **85**, S127.

Medwin, H. & Beaky, M. M. 1989 Bubble sources of the Knudsen sea noise spectra. *J. acoust. Soc. Am.* **86**, 1124–1130.

Medwin, H. & Breitz, N. D. 1989 Ambient and transient bubble spectral densities in quiescent seas and under spilling breakers. *J. geophys. Res.* **94**, 12751–12759.

Medwin, H. & Daniel, A. C. 1990 Acoustical measurements of bubble production by spilling breakers. *J. acoust. Soc. Am.* **88**, 408–412.

Melville, W. K., Loewen, M. R., Felizardo, F. C., Jessup, A. T. & Buckingham, M. J. 1988 Acoustic and microwave signatures of breaking waves. *Nature* **336**, 54–56.

Milne, A. R. 1967 Sound propagation and ambient noise under sea ice. In *Underwater acoustics*, vol. 2 (ed. V. M. Albers), pp. 103–138. New York: Plenum.

Munk, W. H. & Wunsch, C. 1979 Ocean acoustic tomography: a scheme for large scale monitoring. *Deep-Sea Res.* **26**, 123–161.

Olver, F. W. J. 1974 *Asymptotics and special functions*. New York: Academic Press.

Papoulis, A. 1968 *Systems and transforms with applications in optics*. New York: McGraw-Hill.

Pederson, M. A. & Gordon, D. F. 1965 Normal-mode theory applied to short-range propagation in an underwater acoustic surface duct. *J. acoust. Soc. Am.* **37**, 105–118.

Pederson, M. A. & Gordon, D. F. 1970 Theoretical investigation of a double family of normal modes in an underwater acoustic surface duct. *J. acoust. Soc. Am.* **47**, 304–326.

Pekeris, C. L. 1946 Theory of propagation of sound in a half-space of variable sound velocity under conditions of formation of a shadow zone. *J. acoust. Soc. Am.* **18**, 295–315.

Pekeris, C. L. 1948 Theory of propagation of explosive sound in shallow water. *Geol. Soc. Am. Mem.* **27**, 1–117.

Regge, T. 1959 Introduction to complex orbital momenta. *Nuovo Cim.* **14**, 951–976.

Schmidt, H. & Glatettre, J. 1985 A fast field model for three-dimensional wave propagation in stratified environments based on the global matrix method. *J. acoust. Soc. Am.* **78**, 2105–2114.

Sneddon, I. N. 1945 The symmetrical vibrations of a thin elastic plate. *Proc. Camb. phil. Soc.* **41**, 27–43.

Sneddon, I. N. 1946 Finite Hankel transforms. *Phil. Mag.* **37**, 17–25.

Strasberg, M. 1979 Nonacoustic noise interference in measurements of infrasonic ambient noise. *J. acoust. Soc. Am.* **65**, 1487–1493.

Thorpe, S. A. 1982 On the clouds of bubbles formed by breaking wind-waves in deep water, and their role in air-sea gas transfer. *Phil. Trans. R. Soc. Lond.* A **304**, 155–210.

Thorpe, S. A. 1984*a* A model of the turbulent diffusion of bubbles below the sea surface. *J. Phys. Oceanogr.* **14**, 841–854.

Thorpe, S. A. 1984*b* On the determination of K_v in the near-surface ocean from acoustic measurements of bubbles. *J. Phys. Oceanogr.* **14**, 855–863.

Tolstoy, I. & Clay, C. S. 1966 *Ocean acoustics*. New York: McGraw-Hill.

Überall, H. & Nicholas, N. C. 1968 Range focusing in a deep-ocean sound channel with parabolic profile. *J. acoust. Soc. Am.* **44**, 1259–1261.

PHILOSOPHICAL TRANSACTIONS OF THE ROYAL SOCIETY A MATHEMATICAL, PHYSICAL & ENGINEERING SCIENCES

Urick, R. J. 1983 *Principles of underwater sound*, 3rd edn. New York: McGraw-Hill.

Wadhams, P. 1986 The ice cover. In *The Nordic seas* (ed. B. G. Hurdle), pp. 21–84. New York: Springer-Verlag.

Watson, G. N. 1918 Diffraction of electric waves by the earth. *Proc. R. Soc. Lond.* A **95**, 83–99.

Watson, G. N. 1919 Transmission of electric waves round the earth. *Proc. R. Soc. Lond.* A **95**, 546–568.

Watson, G. N. 1958 *A treatise on the theory of Bessel functions*, 2nd edn. Cambridge University Press.

Weston, D. E. 1986 Source depth distribution for uniform intensity in a surface sound channel. *J. acoust. Soc. Am.* **79**, 356–362.

Wood, A. B. 1964 *A textbook of sound*, pp. 360–363. London: Bell and Sons.

Received 26 October 1990; accepted 4 February 1991

PHILOSOPHICAL TRANSACTIONS OF THE ROYAL SOCIETY A MATHEMATICAL, PHYSICAL & ENGINEERING SCIENCES

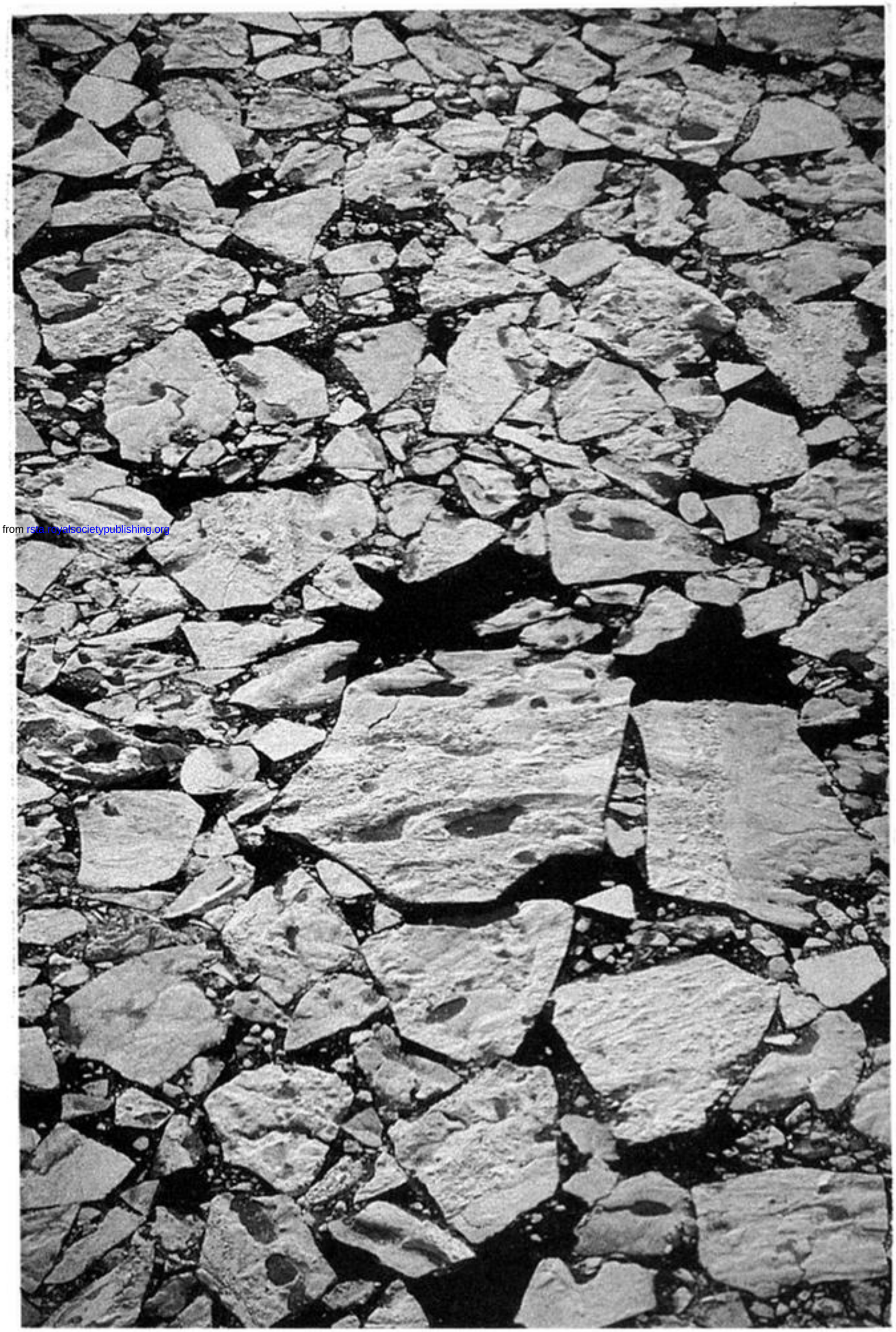

igure 11. Recently fractured ice floes and meltwater pools in the MIZ off the east coast of reenland. The large central floe is about 30 m across. (Aerial photograph by the author.)

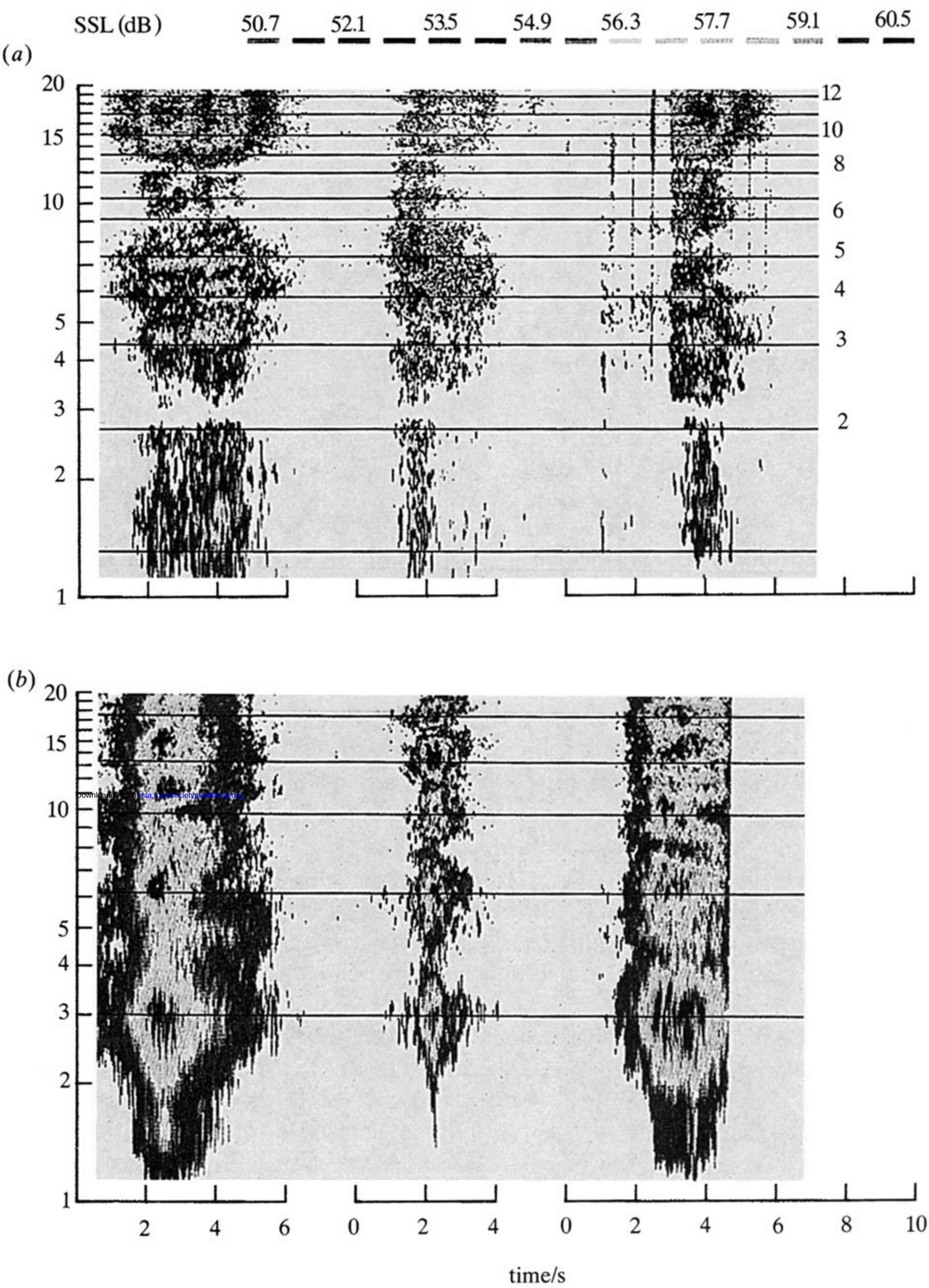

Figure 16. Measured spectra of six wave-breaking events, three in (*a*) FASINEX and three in (*b*) La erouse. (By courtesy of Farmer & Vagle.) The mean slope has been removed from these spectra o emphasize the rather small spectral modulation. The horizontal lines indicate the mode drop-out equencies as calculated by Farmer & Vagle from their exponential profile. Almost identical drop-ut frequencies emerge from the inverse-square theory (cf. figure 17).